UNIVERSITÀ DI GENOVA

Tesi in Fisica

Control of Rydberg states lifetimes with microwaves resonant cavity

Autore
Marco Distefano

Relatore
Dr. Oliver Morsch

ANNO ACCADEMICO 2018/2019

Contents

Introduction

The advent of the modern computational science in the second part of the 20th century led to the creation of algorithms capable of calculating the properties and dynamics of - and hence "simulating" - a variety of physical systems. While this approach is very successful for classical systems, in the world of quantum physics, exact simulations become much more complex and computationally expensive. The fact is that a large number of parameters, such as wave functions, spins etc. are associated to each quantum particle. This would lead to a computational system where it is necessary to associate a huge number of bits for each particle. If we consider for example a system of N spin-1/2-particles, the numbers required to describe it exactly is equal to the number of probability amplitudes for each configuration, which is 2^N. If 40 particles are taken into account, we need to describe $2^{40} \sim 10^{12}$ possible states of the system, which with single precision numbers is already equal to 4 TB. With twice the number of particles, that requirement becomes 10^{12} TB[1]. For comparison, the greatest single memory computer of the world to date, HP's *The Machine*[2], has a memory of 160 TB, ten orders of magnitude less than what would be required to describe the 80 spins mentioned above. As Richard Feynman pointed out in 1980[3], this makes it impossible for any classical computer - present or future - fully to describe the evolution of a large number of coupled quantum systems. This is were the concept of quantum simulators may come into play.
A quantum simulator is an experimental apparatus that is able to simulate other quantum systems. The essential characteristics of such an apparatus is that its Hamiltonian has to be controllable to some extent, and it is necessary to have a good control of the preparation of the initial state and the measurement after a certain time of evolution[4].
This thesis deals with Rydberg atoms[5], which exhibit some interesting properties that make them promising candidates for the realization of quantum simulators. In fact, atoms with an electron excited to a Rydberg state have strong dipole-dipole interactions with each other[6] and long lifetimes. These long lifetimes, and hence also long coherence times, are expected to enable complex quantum simulations. However, the duration of these lifetimes is mostly affected by black body radiation. This is due to the strong coupling of Rydberg atoms with electromagnetic fields and the small difference in energy between neighbouring Rydberg levels, which makes Rydberg atoms highly sensitive to the black body radiation, despite its small intensity[7].

My experimental work consists in the prosecution of the work conducted on Rubidium Rydberg atom lifetimes by M. Archimi during his Ph.D. thesis[8], by L. Di Virgilio, A. Greco and M. Ceccanti during their Master degree theses[9][10][11].
In the literature there are various studies concerning the measurement of Rubidium Rydberg state lifetimes[12][13][14]. These studies considered S, P and D Rydberg states with principal quantum number up to 45. In my experimental work I used a mixed technique that consists of laser pulse excitation, state-selective de-excitation and field ionization of Rydberg states. With this technique we are able to measure S, P and D Rydberg state lifetimes with principal quantum number up to 110. The main limitation for our measurements is the presence of a small electric field that we must compensate in order to minimize the Stark shift. Apart from the electric field, we are only limited by the linewidth of the excitation laser. Previous experiments in our laboratory[8][9][10][11] revealed significant deviations in Rydberg atom lifetimes from the expected theoretical values[15]. Rydberg state lifetimes with angular momenta S and P with different principal quantum numbers n were measured. Shorter lifetimes were observed for Rydberg atoms of different l whose black body radiation induced frequencies were in the same frequency ranges. Therefore, these deviations were attributed to deviations of the mode density of the black body radiation from the theoretical mode density predicted by Planck's formula. In fact, in the region of the apparatus where Rydberg atoms are produced, the finite sized geometry of the surroundings acts as resonant cavity and modifies considerably the mode density of the black body radiation.
At the beginning of my experimental work in the laboratory, I performed measurements of Rydberg D state lifetimes to confirm the hypothesis regarding the origin of these deviations. I confirmed the correlation between the deviations of lifetimes and the modified mode density of the black body radiation also for Rydberg D states.
Even though the reductions of lifetimes due to the enhancement of certain modes was the main phenomenon observed, for certain Rydberg states a small enhancement of their lifetimes was observed. Indeed, in the literature there are both experimental and theoretical studies on the enhancement of Rydberg lifetimes[16][17]. This led us to the idea of exploiting this influence of those modified mode densities on Rydberg lifetimes. Instead of producing shorter lifetimes, the idea was to extend them, by suppressing the modes associated to the black body induced transitions. In fact, the density of modes of a resonant cavity shows regions of suppressed modes between the cavity resonances, as well as below the cut-off frequency[18]. To produce such effects, an additional resonant cavity had to be implemented in the apparatus.
This idea was applied during my experimental work, after the measurements of D state lifetimes. I designed and supervised the fabrication of the resonant cavity elements that we added to the apparatus. I dealt with the adjustment of the ions detection and the electric field compensation with these new elements. I took several sets of Rydberg S state lifetimes measurements with different configurations of the cavity. Finally I analysed the results by calculating the rates of the transitions induced by the black body radiation.

The contents of this thesis are organized as follows: chapter 1 concerns the theory background of the aspects regarding my experimental work. It begins with an overview of Rydberg atom theory and their properties, with particular attention given to on Rydberg atom lifetimes. Afterwards, I show the calculations that lead to the theoretical expression of the mode density of the black body radiation, i.e. Planck's formula. I subsequently explain how this expression can differ from the Planck result for finite sized boundary system. In the end of the chapter I deal with the problem of an open resonant cavity, introducing the definition of Q factor.
Chapter 2 focuses on the experimental apparatus, which consist mainly of the Magneto-optical trap. The chapter continues with the description of the two-photon excitation technique that allows us to excite single Rydberg states. Then I explain how these Rydberg atoms are detected with our field ionization technique. I briefly deal with the compensation of the stray electric field. The chapter ends with the accurate description of the additions to the apparatus needed to produce a resonant cavity in the microwave regime, in order to control Rydberg state lifetimes.
In chapter 3 the experimental results are shown. The chapter begins with the description of the lifetime measurement technique and the methods for calculating rates of black body radiation induced transitions. The chapter continues showing the previous results of the Rydberg S and P lifetime measurements, and comparing it with my measurements of the D state lifetimes. Then I move to the results obtained by the lifetimes measurements with the presence of the resonant cavity. I finally present the results of the data analysis performed on the measurements, and comment them.

Chapter 1

Theoretical Background

1.1 Introduction

In this chapter I will introduce the theoretical aspects of my thesis, which mainly concerns Rydberg atoms, black body radiation (BBR), resonant cavities and how the these cavities can modify the BBR spectrum and influence transitions rates between Rydberg states.
Rydberg atoms, i.e. atoms with one electron excited to a high-lying state, have several peculiar properties. One of these are their lifetimes, which can be hundreds of times greater than those of low-lying states[1]. At $T = 300K$, those lifetimes are mostly determined by the transitions between Rydberg states induced by the black body radiation. The density of modes of this radiation is described by Planck's formula. This formula is considered valid when the separation between the walls of the system is much greater than the wavelengths of the radiation. However, in systems with finite sized boundaries, the mode spectrum can differ radically from the smooth distribution of the density of modes of Planck's formula, showing regions of enhanced and suppressed modes according to the harmonics of the resonant cavity.

1.2 Rydberg atoms

In this section I will discuss the theory of Rydberg atoms as far it concerns my work.
A Rydberg atom is an atom of any species in which the outer electron is excited to a high-lying state, i.e. with a high principal quantum number n[19]. This means that the average distance between the nucleus and electron is large enough that the wave function of the electron can be approximated to the wave function of the Hydrogen atom electron. States with high orbital angular momentum, where the electron spends most of the time far away from the nucleus, have practically the same

[1] for the states with principal number from $n = 65$ to $n = 110$ that we considered for our experiments.

wave functions and energy levels as the H atom. By contrast, for low l, the electron perceives more the core-size of the rest of the atom. Consequently, the energy levels deviate from the ones of a H atom according to an empirical parameter called *quantum defect* $\delta_{n,l,j}$. This parameter depends on the principal quantum number n, on the angular momentum quantum number l and on the total angular momentum quantum number j. The parameter takes into account the lack of screening of the nuclear charge by the other core electrons for states with low l and varies depending on the species. The energy levels of the Rydberg states are shifted depending on their quantum numbers n, l and j (Table 1.1), following the equation

$$\epsilon_{nlj} = -R_y \frac{1}{(n - \delta_{n,l,j})^2}, \tag{1.1}$$

Where R_y is the Rydberg universal constant and we define $n^* = (n - \delta_{n,l,j})$.
The fact that $\delta_{n,l,j}$ has significantly different values for different nL causes such energy shifts that a nS state has a lower energy than the n' states with $l = 3$ and $n' = n - 3$.
Regarding the other properties of the Rydberg atoms, the formulas for the H atom apply also to Rydberg atoms with the substitution of the principal quantum number with n^* (Table 1.2). In the following section I will expose some of those properties that have been most important for my work.

Quantum defect $\delta_{n,l,j}$	
State	$\delta_{n,l,1/2}$
85S	3.1312
85P	2.6549
85D	1.3464
85F	0.0165
85G	0.0041

Quantum defect $\delta_{n,l,j}$	
nS State	$\delta_{n,0,1/2}$
40S	3.13131
60S	3.13124
80S	3.13121
100S	3.13120

Table 1.1: Quantum defects for different orbital momentum of the same n Rubidium Rydberg state (left-hand side) and quantum defects of different nS Rydberg states (right-hand side). As it can be seen from the left table, already for F states the quantum defect becomes negligible.

Property	Scaling factor	Rb(5S)	Rb(85S)
Binding Energy	n^{*-2}	4.18 eV	2.06 meV
Level spacing	n^{*-3}	2.50 eV (5S-6S)	48.7 μeV
Lifetime ($T = 300$ K)	n^{*3}	26.2 ns ($5P_{3/2} - 5S_{1/2}$)	235 μs
Polarizability [MHz$\frac{\text{cm}^2}{\text{V}^2}$]	n^{*7}	79.4×10^{-9}	~ 2143
Orbit radius	n^{*2}	$\sim 29.8 \times 10^{-5}$ μm	0.532 μm

Table 1.2: Properties of Rydberg atoms as function of $n^* = (n - \delta_{n,l,j})$. Data for the $5S$ are from [20], while those for the $85S$ are calculated using an open-source code[21].

1.2.1 Stark shift

In this section I will deal with the interaction between Rydberg atoms and a constant electric field, which results in the well-known energy level shift, called *Stark shift*. In our experiments we have to take into account this phenomenon very carefully, as for sufficiently great electric field we no longer are able to excite single Rydberg states but mixed states.
Let's start from the Hamiltonian:

$$\hat{H}' = \hat{H}^0 + \hat{V}, \tag{1.2}$$

Where $\hat{H}^0$ is the Hamiltonian of the Rydberg atom with $E = 0$, and $\hat{V}$ the interaction term between the atom and the electric field. If the electric field is uniform, we can write the interaction term as $\hat{V} = -E\hat{d}_z$. If the electric field is small enough, that is $E\langle\hat{d}_z\rangle \ll \Delta\epsilon$, we can apply to the Hamiltonian the perturbation theory [22]. Now we have two distinct cases: whether we shall consider states with defined angular momentum or states that are degenerate in l.
In the first case we have a well-defined parity of the wave function. Let's consider for instance a S state. This means that the average dipole element $\langle nS|\,\hat{d}_z\,|nS\rangle$ is zero, therefore the energy shift has no linear dependence on the field. Calculating the perturbation to the second order, we get that the state energy level shift is

$$\delta_\epsilon^{(2)} = E^2 \sum_k \frac{|\,\langle k|\,\hat{d}_z\,|nS\rangle\,|^2}{\epsilon_k - \epsilon_{nS}}. \tag{1.3}$$

Therefore the energy shift has a quadratic dependence on the field magnitude. Defining the *polarizability* α of the state as $\alpha = -2\frac{\delta_\epsilon^{(2)}}{E^2}$, we get:

$$\alpha = -2\sum_k \frac{|\,\langle k|\,\hat{d}_z\,|nS\rangle\,|^2}{\epsilon_k - \epsilon_{nS}} \tag{1.4}$$

Using the scaling law for dipole matrix elements between neighbouring states $\langle n' \sim n|\,\hat{d}_z\,|nS\rangle \propto n^{*2}$ and the scaling law for the difference of energies between neighbouring states from Table 1.2, we deduce that $\alpha \propto n^{*7}$.

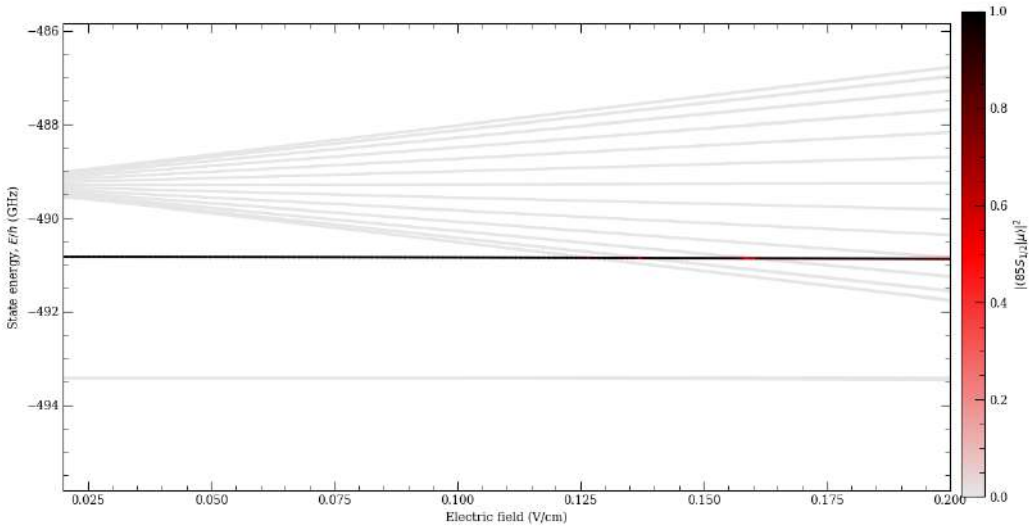

Figure 1.1: Diagram of Rydberg states calculated with ARC[21]. $85S$ state level is shown below the $n = 82$ manifold. The crossing between the manifold and the $85S$, i.e. the Inglis-Teller limit, is located at about $E = 125\,\mathrm{mV/cm}$

Regarding l-degenerate states, we have to apply degenerate perturbation theory. As we can see from Table 1.1, for $l > 4$ the quantum defect does not lift the degeneracy of the energy levels (1.1), which goes as $n^2 - 16$ (for $n = 80$ we get 6384 degenerate levels).
If we consider a basis $\{e\} = n, l, j$, with a fixed n and $4 \leq l \leq n - 1$, and calculate the matrix associated with the operator $\hat{V} = -E\hat{d}_z$, we will get off-diagonal matrix elements for pair states with $\Delta l = \pm 1$. At the first order diagonalising the matrix we get the first order energy shift as its eigenvalues, which is linear in the electric field.
Since the high degeneracy of the levels with $l > 4$, their levels splitting results in an almost continuum of states whose extension grows as a function of the field in the shape of a fan (Figure 1.1). We call these levels *manifold*.
Because the energy shifts of degenerate states in the manifold are a result of a first order correction, they grow more rapidly as a function of E than the shifts of non-degenerate states. This means that there is a field magnitude where the degenerate states will cross the non-degenerate ones, causing a mixing between the states. This field value is called Inglis-Teller limit.

1.2.2 Field ionization

An important characteristic of Rydberg atoms is their ionization threshold, i.e. the energy needed to bring the excited electron from a Rydberg state to the continuous energy spectrum as a free particle (Figure 2.2 of chapter 2). Those thresholds are much smaller than the threshold of the low-lying states, as a consequence of the small binding energy of Rydberg states (Table 1.2).
To get an expression for the ionization threshold, let's consider a simplified one dimensional and classical model where an electron is attracted by Coulomb potential and with an electric field in the z direction:

$$U_{el} = -\frac{e^2}{4\pi\varepsilon_0|z| + eEz} \tag{1.5}$$

This potential has a local maximum for $z_{max} = -\sqrt{\frac{e}{4\pi\varepsilon_0 E}}$, i.e. $U_{el}^{max} = 2e\sqrt{\frac{eE}{4\pi\varepsilon_0}}$. A classical electron is in a bound state only for energies lower than this maximum potential. Therefore if we substitute U_{el} with the expression for the binding energy of a Rydberg atom, we get the minimum electric field to ionize an n Rydberg state:

$$E_{thr} = \frac{m_e^2 e^5}{16(4\pi\varepsilon_0)^3\hbar^4}\frac{1}{n^{*4}} \tag{1.6}$$

Thus the ionization threshold goes as n^{*-4} and for the Rydberg used in our experiments it takes values of few tens of V/cm, which can be easily reached with our apparatus (see section 2.4).

1.2.3 Rydberg lifetimes

One of the most peculiar properties of Rydberg atoms is their lifetimes. Rydberg state lifetimes are much longer than lifetimes of low-lying states, following the scaling factor of Table 1.2. We will calculate this scaling factor in this section.
The lifetime of an isolated Rydberg atom equals to the sum of the rates of every possible spontaneous emission rate. The spontaneous emission rate between $|nl\rangle$ and $|n'l'\rangle$ is given by the Einstein coefficients [22]:

$$A_{nlj,n'l'j'} = \frac{4e^2\omega_{nlj,n'l'j'}^3}{3\hbar c^3}\frac{l_{max}}{2l+1}R_{nlj,n'l'j'}^2, \tag{1.7}$$

where $R_{nlj,n'l'j'}^2 = |\langle nl|\, r\, |n'l'j'\rangle|$ is the radial matrix element of the electric dipole transition, l_{max} is the largest angular momentum number of l and l' and $\omega_{nlj,n'l'j'} = |\epsilon_{nlj} - \epsilon_{n'l'j'}|/\hbar$.
If we consider a state with energy ϵ_{nlj}, a spontaneous decay can only happen to states with lower energy. Therefore, the total spontaneous decay rate is:

$$\Gamma^{(spon)} = \sum_{\epsilon_{n'l'j'} < \epsilon_{nlj}} A_{nlj,n'l'j'} \tag{1.8}$$

Regarding Equation (1.7), the factor $\omega^3_{nlj,n'l'j'}$ makes the spontaneous decay processes happen mostly to low-lying states. This is because Rydberg levels are very close in frequency compared to the low-lying levels. So this factor can be considered constant in n^*. The radial matrix element, on the other hand, exhibits a $\propto n^{*-3}$ trend, so the lifetime for an isolated Rydberg atom grows as n^{*3}.

However, in order to get the actual lifetime of a non-isolated Rydberg atom, we have to take into account also the transitions between adjacent Rydberg levels induced by black body radiation emitted by the apparatus that surrounds the atoms. The spectral density of this radiation, for a temperature T, is expressed by the well-known Planck formula:

$$u_\omega = \frac{\hbar}{\pi^2 c^3} \frac{\omega^3}{e^{\beta\hbar\omega} - 1}, \tag{1.9}$$

where $\beta = 1/k_B T$ (k_B is the Boltzmann constant). At the laboratory temperature of $T = 300\,\mathrm{K}$ and at the transition frequencies between the Rydberg levels considered by our experiments, the black body radiation has a small intensity. Let's consider for instance a typical transition frequency between Rydberg states considered by our experiments, i.e. $\nu = 5\,\mathrm{GHz}$. Then we consider a frequency interval of $\Delta\nu = 500\,\mathrm{MHz}$, which is approximately equal to the range of the frequencies of the transitions that have the greatest black body induced rates. With these values we obtain an energy per unit of volume of $10^{-8}\,\mathrm{J/m^{-3}}$. On the other hand, the dipole matrix elements between the starting neighbouring Rydberg levels are large, for instance $\langle 85S_{1/2}|\, e\mathbf{r}\, |85P_{3/2}\rangle \sim 10^{32}\,\mathrm{Cm}$[2]. Thus the coupling between the black body radiation and those levels is significant, resulting in a black body induced transition rate of about 2.5 kHz. From the Equation (1.9) the black body radiation is null at $T = 0$, and thus we can define the spontaneous rate of (1.8) as the total rate at zero temperature: $\Gamma^{tot}(T = 0\,\mathrm{K}) = \Gamma^{(spon)}$.

We can express the BBR-induced transition rates with the Einstein B coefficients and the density of modes in Planck's formula at the transition frequency:

$$\Gamma^{(BBR)}_{nlj,n'l'j'} = B_{nlj,n'l'j'} \cdot u_\omega(\omega_{nlj,n'l'j'}, T) = A_{nlj,n'l'j'} \frac{1}{e^{\beta\hbar\omega_{nlj,n'l'j'}} - 1}, \tag{1.10}$$

Where we exploited the Einstein coefficients relation $A_{1,2} = B_{1,2} \frac{2\hbar\omega^3}{\pi c^3}$. In the sum of all BBR rates we have to take into account all transitions, as thermal radiation photons can both be absorbed and cause stimulated emissions, which is respectively equal to transitions to higher levels and lower levels.

[2]Dipole matrix element calculated with the ARC libraries[21].

Hence we get the overall lifetime of a Rydberg atom as:

$$\tau_{nlj}(T) = \left(\sum_{\epsilon_{n'l'j'} < \epsilon_{nlj}} A_{nlj,n'l'j'} + \sum_{n'l'j'} \frac{A_{nlj,n'l'j'}}{e^{\beta\hbar\omega_{nlj,n'l'j'}} - 1} \right)^{-1} = \left(\Gamma^{(spon)} + \Gamma^{(BBR)} \right)^{-1}. \quad (1.11)$$

Now we would like to know how the $\Gamma^{(BBR)}$ scales with n^*. Firstly, we replace the Einstein A coefficient with its definition:

$$\Gamma^{(BBR)}_{nlj} = \frac{4e^2}{3\hbar c^3} \sum_{n'l'j'} \frac{l_{max}}{2l+1} R^2_{nlj,n'l'j'} \frac{\omega^3_{nlj,n'l'j'}}{e^{\hbar\omega_{nlj,n'l'j'}/k_BT} - 1}. \quad (1.12)$$

We observe that the contribution of transitions to states with n' far away from the n of the initial state is suppressed by the exponential in the denominator in 1.12, and only the transitions to states with close n' remain. Their frequencies scale accordingly to energy levels as:

$$\omega_{n,n+1} \propto \frac{1}{n^{*2}} - \frac{1}{(n^*+1)^2} \sim \frac{1}{n^{*3}} \quad (1.13)$$

However, for the Rydberg states used in our laboratory, i.e. with $n > 60$, at $T \sim 300\,\mathrm{K}$ we have $k_BT >> \hbar\omega$. expanding to first order the exponential of (1.12), we get:

$$\Gamma^{(BBR)}_{nlj} = \frac{4e^2 k_B T}{3\hbar c^3} \sum_{n'l'j'} \frac{l_{max}}{2l+1} R^2_{nlj,n'l'j'} \omega^2_{nlj,n'l'j'}. \quad (1.14)$$

But we have that $\frac{1}{3\pi} R^2_{nlj,n'l'j'} \omega_{nlj,n'l'j'} = f_{nl,n'l'}$, which is the oscillator strength. Consequently, for a known sum rule [19], we know that:

$$\sum_{n'l'j'} \omega_{nlj,n'l'j'} f_{nl,n'l'} \sim \frac{2}{3} n^{*-2}. \quad (1.15)$$

So the BBR rate scales as n^{*-2}, and for the Rydberg levels considered in this thesis with n above 60, it becomes the predominant decay rate, as can be seen in Table 1.3.

1.3 Planck's formula for black body radiation

In this section I will introduce and demonstrate Planck's formula for the black body radiation, as a basis point to introduce the deviations from this formula with a finite sized system.
Firstly, it is necessary to show how it is possible to express the electromagnetic field in a volume as set of harmonic oscillators, which will be a fundamental statement for the further analysis.

nS	$\Gamma^{(spon)}$ kHz	$\Gamma^{(BBR)}$ kHz
60	4.34	3.98
70	2.67	3.30
80	1.76	2.67
90	1.22	2.20
100	0.88	1.83

Table 1.3: BBR rates and spontaneous rates are shown for Rydberg nS states with different principal quantum numbers. Above $n = 60$, BBR rate becomes greater than the spontaneous rate. These values were calculated using ARC libraries[21].

1.3.1 Electromagnetic fields as collection of harmonic oscillators

Let's start with the Maxwell equations in vacuum[23]:

$$\nabla \cdot \mathbf{E} = 0 \qquad \nabla \times \mathbf{E} = -\frac{\partial \mathbf{B}}{\partial t} \quad \nabla \cdot \mathbf{B} = 0 \qquad \nabla \times \mathbf{E} = \mu_0 \varepsilon_0 \frac{\partial \mathbf{E}}{\partial t} \tag{1.16}$$

From these it is possible to get the wave equations:

$$\left(\frac{1}{c^2} - \nabla^2\right) \mathbf{E}(\mathbf{r}, t) = 0 \quad \left(\frac{1}{c^2} - \nabla^2\right) \mathbf{B}(\mathbf{r}, t) \qquad = 0, \tag{1.17}$$

Where $c = 1/\mu_0 \varepsilon_0$.
Let's consider a cubical volume with $V = L^3$, and look for solutions in the following form:

$$a(t)\mathbf{u}(\mathbf{r}) \tag{1.18}$$

Substituting in (1.17), we get:

$$\frac{\partial^2 a}{\partial t^2} + \omega^2 a(t) = 0 \Longrightarrow a(t) = a_0 e^{-i\omega t}$$

and

$$\nabla^2 \mathbf{u} + \frac{\omega^2}{c^2}\mathbf{u} = \mathbf{0} \Longrightarrow \frac{1}{\sqrt{V}} e^{i\mathbf{k}\cdot\mathbf{r}} \hat{e}_{\mathbf{k}}, \tag{1.19}$$

Where $|\mathbf{k}| = k = \frac{\omega}{c}$. Applying the condition of no divergence on $\mathbf{u}$, one gets $\hat{e}_{\mathbf{k}} \cdot \mathbf{k} = 0$. This means that for each mode it is possible to have two polarizations, perpendicular to each other and to $\mathbf{k}$. Therefore, the solution of Equation (1.19) is:

$$\mathbf{u}_{\mathbf{k},s}(\mathbf{r}) = \frac{1}{\sqrt{V}} e^{i\mathbf{k}\cdot\mathbf{r}} \hat{e}_{\mathbf{k},s}, \tag{1.20}$$

Where s is the polarization of the mode. So we got a orthonormal basis of the electromagnetic field. Indeed:

$$\int_V d\mathbf{r}\left[\mathbf{u}_{\mathbf{k},s}(\mathbf{r})\cdot\mathbf{u}_{\mathbf{k}',s'}(\mathbf{r})\right]=\delta_{\mathbf{k},\mathbf{k}'}\delta_{s,s'} \tag{1.21}$$

Now it's possible to expand the fields as:

$$\mathbf{E}(\mathbf{r},t)=-\frac{1}{\sqrt{\varepsilon_0}}\sum_{\mathbf{k},s}p_{\mathbf{k},s}(t)\mathbf{u}_{\mathbf{k},s}(\mathbf{r}) \tag{1.22}$$

$$\mathbf{B}(\mathbf{r},t)=-\frac{1}{\sqrt{\varepsilon_0}}\sum_{\mathbf{k},s}q_{\mathbf{k},s}(t)\mathbf{v}_{\mathbf{k},s}(\mathbf{r}), \tag{1.23}$$

Where from the Maxwell equations (1.16) we get $\mathbf{v}_{\mathbf{k},s}(\mathbf{r})=\nabla\times\mathbf{u}_{\mathbf{k},s}(\mathbf{r})$ and that p and q satisfy the harmonic oscillator equation:

$$\frac{dq_{\mathbf{k},s}(t)}{dt}=p_{\mathbf{k},s}(t)\qquad\frac{dp_{\mathbf{k},s}(t)}{dt}=-\omega_{\mathbf{k}}^2q_{\mathbf{k},s}(t), \tag{1.24}$$

where $\omega_{\mathbf{k}}=c\mathbf{k}$.
Finally, it's possible to evaluate the electromagnetic energy:

$$\mathcal{H}=\int_V d\mathbf{r}\left(\frac{\varepsilon_0}{2}\mathbf{E}\cdot\mathbf{E}+\frac{1}{2\mu_0}\mathbf{B}\cdot\mathbf{B}\right)=\frac{1}{2}\sum_{\mathbf{k},s}\left(p_{\mathbf{k},s}^2+\omega_{\mathbf{k}}^2q_{\mathbf{k},s}^2\right) \tag{1.25}$$

Therefore, the energy can be expressed as a sum of harmonic oscillators.

1.3.2 Photon gas

With the consideration of the previous section, it is possible to handle correctly the electromagnetic radiation in a box of $V=L^3$ volume.
For each photon there is a related wave function in the form $\phi_{\mathbf{k},s}(\mathbf{r})=\frac{1}{\sqrt{V}}e^{i\mathbf{k}\cdot\mathbf{r}}\hat{e}_{\mathbf{k},s}$. For the boundary conditions, the wave vectors can assume only values that satisfy the relation:

$$(k_x,k_y,k_z)=\frac{2\pi}{L}(l_x,l_y,l_z),\quad l_x,l_y,l_z=0,\pm1,\pm2,\dots \tag{1.26}$$

The energy of an harmonic oscillator will be related to each mode, as shown in the previous section:

$$E_{\mathbf{k},s}=\left(n_{\mathbf{k},s}+\frac{1}{2}\right)\hbar\omega_{\mathbf{k},s}, \tag{1.27}$$

where $n_{\mathbf{k},s}$ is the number of photons with wave vector $\mathbf{k}$, polarization s and energy $\hbar\omega_{\mathbf{k},s}$.
Now, remembering that the average number of particles with energy equals to $\hbar\omega_{\mathbf{k},s}$, is expressed

as [3]:

$$\langle n_{\mathbf{k},s} \rangle = \frac{1}{e^{\frac{\hbar\omega_{\mathbf{k},s}}{k_B T}} - 1}, \tag{1.28}$$

we get the mean energy of the system as:

$$\langle E \rangle = \sum_{\mathbf{k},s} \left(\langle n_{\mathbf{k},s} \rangle + \frac{1}{2} \right) \hbar\omega_{\mathbf{k},s} = 2 \sum_{\mathbf{k}} \left(\frac{1}{2}\hbar\omega_{\mathbf{k}} + \frac{\hbar\omega_{\mathbf{k}}}{e^{\frac{\hbar\omega_{\mathbf{k}}}{k_B T}} - 1} \right), \tag{1.29}$$

where we exploited the fact that both polarizations give the same contribution. In order to go from the sum to the integral it is necessary to introduce the function $g(k)dk$, where $g(k)$ is the density of states. Let's consider a spherical shell of radius k and thickness dk, that is extended only over the first octant, since only those $\mathbf{k}$ vectors contribute. This volume can be expressed as:

$$\frac{1}{8} \times 4\pi k^2 dk \tag{1.30}$$

From Equation (1.26) one knows that the volume in k-space occupied per allowed state is $(2\pi/L)^3$, hence:

$$g(k)dk = \frac{\frac{1}{8} \times 4\pi k^2 dk}{(2\pi/L)^3} = \frac{V k^2 dk}{\pi^2}. \tag{1.31}$$

Then, the integral form of Equation (1.29) becomes:

$$\langle E \rangle = 2 \int_0^\infty dk \left(\frac{\hbar c k}{e^{\frac{\hbar c k}{k_B T}} - 1} g(k) \right) = 2 \frac{V}{(2\pi)^3} \int_0^\infty dk \left(4\pi k^2 \frac{\hbar c k}{e^{\frac{\hbar c k}{k_B T}} - 1} \right) =$$
$$= \frac{V\hbar}{\pi^2 c^3} \int_0^\infty d\omega \left(\frac{\omega^3}{e^{\frac{\hbar\omega}{k_B T}} - 1} \right),$$

where the ground energy part, that is equal to the first term of the sum in (1.29), has been left out, as it doesn't depend on the temperature. Consequently, we can define a spectral energy density in the following form

$$u_\omega = \frac{\hbar V}{\pi^2 c^3} \frac{\omega^3}{e^{\beta\hbar\omega} - 1}, \tag{1.32}$$

where $\beta = 1/k_B T$. So that the overall energy density is defined as

$$u = \frac{\langle E \rangle}{V} = \int_0^\infty u_\omega d\omega. \tag{1.33}$$

This spectral density describes the black body radiation (BBR) spectrum. There are alternative forms as u_ν (where $\nu = \omega/2\pi$) and u_λ (where $\lambda = 2\pi c/\omega$) (the plot of these two functions can be

[3] This can be obtained by the quantum canonical ensemble theory [23].

seen in Figure 1.2):

$$u_\nu = \frac{8\pi h}{c^3}\frac{\nu^3}{e^{\beta h\nu}-1} \qquad u_\lambda = \frac{8\pi hc}{\lambda^5}\frac{\nu^3}{e^{\frac{\beta h}{\lambda}}-1} \tag{1.34}$$

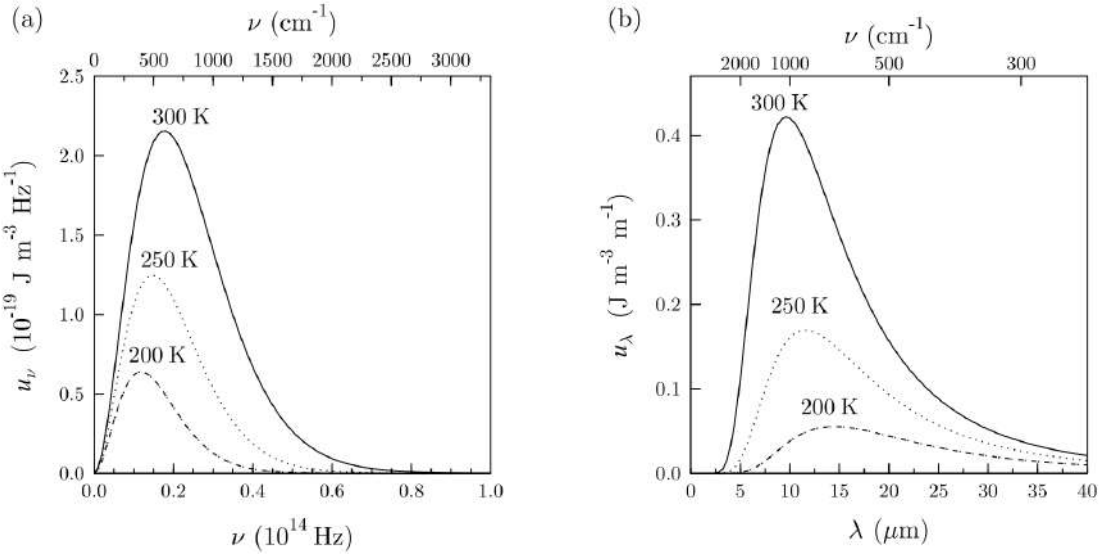

Figure 1.2: The black body spectral density plotted as a function of frequency ν (a) and wavelength λ (b). Figure taken from [23]

1.4 Resonant cavity

1.4.1 BBR deviations due to finite sized geometry

The spectral density for BBR in the previous section has been derived by making an assumption. In Equation (1.3.2), the mean energy of oscillators in the system (1.29) was set to be equal to the number of modes given by the expression of the density of states (1.31). In fact, the formulation for the mean energy in (1.28) can be considered always correct, as in every system the number of atoms, that correspond to the oscillators, is very large. The density of modes (1.31), on the other hand is a good approximation only for a cavity with a large enough volume compared to the wavelength of interest.
Indeed, Planck's formula can be considered valid only if

$$1 \gg \Delta\lambda/\lambda \gg (\lambda/L)^3, \tag{1.35}$$

where $\Delta\lambda$ is defined as $\Delta\lambda = \lambda\Delta\nu/\nu$, i.e. the wavelength interval corresponding to the frequency interval where the number of modes are counted [24]. Otherwise, it is necessary to take into account how the frequency modes are modified by the presence of the finite size cavity. In the case of our experiments for instance, if we consider the dimension of the system, where L is of the order 10^{-1} m, a typical frequency associated to the BBR-induced transitions of Rydberg levels of 5 GHz, and $\Delta\nu = 500$ MHz, we obtain $(\lambda/L)^3 = 5 \times 10^{-1}$, while $\Delta\lambda/\lambda = 1 \times 10^{-1}$. So the conditions of (1.35) are not satisfied. Also, it is clear that for a cavity of that size, there is a cut-off frequency of around 1 GHz, below which there are no allowed cavity modes. Since this cut-off frequency is close to the transition frequencies we are interested in, we expect to see significant deviations from the density of modes assumed in the derivation of Planck's formula. Therefore it's necessary to treat the box of the system with the resonant cavity theory.
Let's consider a cavity with L_x, L_y, L_z sides. The resonant frequencies will be

$$f_{\{n\}} = \frac{c}{2}\sqrt{\left(\frac{n_x}{L_x}\right)^2 + \left(\frac{n_y}{L_y}\right)^2 + \left(\frac{n_z}{L_z}\right)^2}, \tag{1.36}$$

where $\{n\}$ is a triplet of n_x, n_y and n_z. If the modes are sorted in ascending order, it's possible to count the number of modes as every combination of the $\{n\}$ triplet[4] up to a frequency f:

$$N(f) = \sum_{\{n\}|f_{\{n\}} \leq f} 1 \tag{1.37}$$

[4]It is necessary to exclude the cases where $n_i = 1$ and $n_j = n_k = 0$, where i, j, k are any combination of x, y, z. This is because these modes are forbidden by the resonant cavity theory[25].

And we obtain the number of modes calculated with (1.37) within a frequency range $\Delta\nu$ as:

$$N(\nu) = \sum_{\nu < f_\nu \leq \Delta\nu} 1 \tag{1.38}$$

If the oscillator mean energy $\Theta_{\{n\}}(T, f_{\{n\}}) = hf_n / \left(e^{\frac{hf_{\{n\}}}{K_B T}} - 1 \right)$ is assigned to each mode, one can evaluate the total energy as

$$U(T, f) = \sum_{n | f_n \leq f} \Theta_{\{n\}}(T, f_{\{n\}}). \tag{1.39}$$

Then, in order to compare the energy density to Planck's formula, we need to calculate the degeneracies of the modes, i.e. the number of modes between one resonant frequency and the following one (Δf):

$$\Delta N(f) = \sum_{n | f < f_n \leq f + \Delta f} 1 \tag{1.40}$$

Finally, the spectral energy density expressed in J/Hz is

$$u(T, f) = \Theta(T, f) \frac{\Delta N(f)}{\Delta f}. \tag{1.41}$$

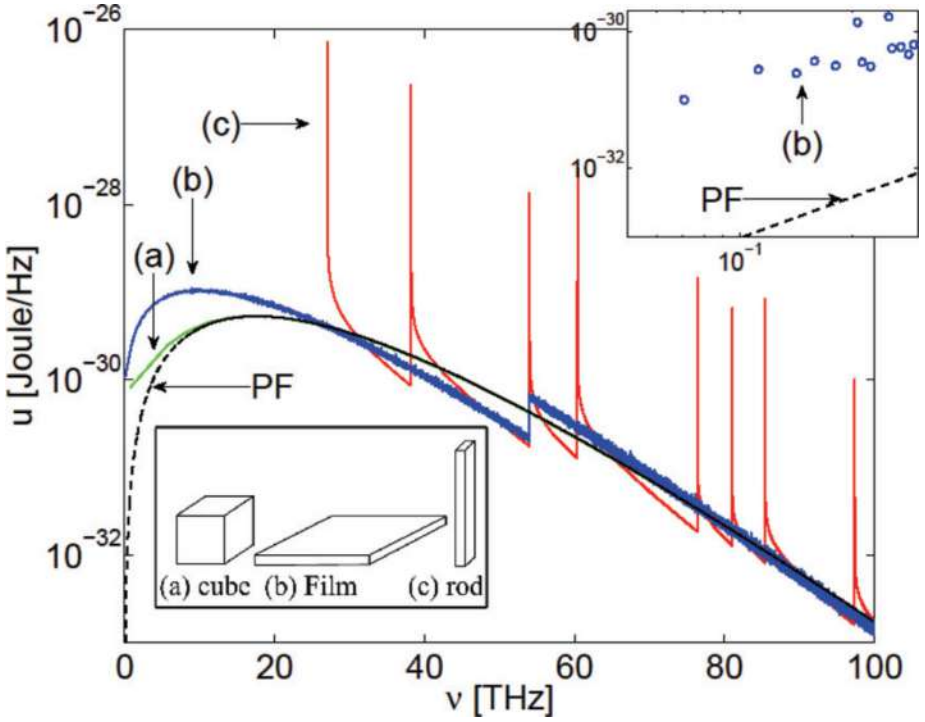

Figure 1.3: Comparison between energy density for different geometries with the same volume ($0.025\,\mathrm{mm}^3$) and the one obtained from Planck's formula. In the inset at top right the energy density of a film for low frequencies, where the modes are discrete and don't form a continuum as for higher frequencies. Figure taken from [18]

Now it is possible to compare this expression with the energy density of Planck's formula. In Figure 1.3[18] the deviations from Planck's formula for finite geometries are shown. The most significant trend regarding our apparatus is the one with the geometry of a rod, as both the silica cell where Rydberg atoms are created and the resonant cavity that was added to the apparatus have a similar geometry[5]. Several peaked resonances in the density spectrum can be observed, where the BBR modes are enhanced significantly and much greater than the BBR modes of Planck's formula. On the other hand, between those resonances there are regions were the modes are suppressed and smaller than those of Planck's formula.

In our experiments we want to exploit this last property to suppress the BBR-induced transitions and therefore extend Rydberg lifetimes. Nevertheless, we have to consider some corrections to the theoretical trend of the mode density. In fact, the trends of Figure 1.3 are clearly calculated with no energy losses and therefore with a high quality factor (Q).

[5]The geometry of the apparatus is explained in (2.6.1), while the added resonant cavity is described in (2.6.2) and (2.6.3)

Let's consider an open resonant cavity with width of the walls that is comparable to the wavelength under consideration, or a cavity where the walls are poorly reflective. Both of these properties lead to significant energy losses and a smaller quality factor. In the following section I will show how these losses cause a broadening of the resonances calculated before and consequently also a narrowing of the regions with suppressed modes.

1.4.2 Q factor

Let's assume we produce an electromagnetic excitation inside a resonant cavity[25]. The Q factor is defined as 2π times the ratio of the energy stored to the energy loss per cycle:

$$Q = \omega_0 \frac{U}{P_{loss}}, \tag{1.42}$$

Where ω_0 is the ideal resonance frequency without losses. Applying the conservation of energy, we know that the power dissipated equals to the negative of the time rate of change of stored energy:

$$P_{loss} = \frac{dU}{dt} = -\frac{\omega_0}{Q} U \tag{1.43}$$

This differential equation holds as solution:

$$U(t) = U_0 e^{-\frac{\omega_0}{Q} t} \tag{1.44}$$

So the energy stored decays exponentially with a time scale proportional to Q. Therefore if we consider the field oscillations in the cavity with frequency $\omega_0 + \Delta\omega$, these will be damped as follows:

$$E(t) = E_0 e^{-\frac{\omega_0}{Q} t} e^{-i(\omega_0 + \Delta\omega)t} \tag{1.45}$$

Applying a Fourier transform to this expression, we obtain that the frequency distribution of the energy in the cavity has Lorentzian resonant shape:

$$|E(\omega)|^2 \propto \frac{1}{(\omega - \omega_0 - \Delta\omega)^2 + (\omega_0/2Q)^2}, \tag{1.46}$$

where the half width Γ equals to ω_0/Q, and consequently $Q = \omega_0/\Gamma = \omega_0/\Delta\omega$. So if we get back to the Q factor definition, if we have significant energy losses compared to the energy stored, Q assumes small values, which is equal to a broadening of the resonances.

In our experiments it was not possible to evaluate exactly the Q factor of our resonant cavity. In the literature[26] there are exact calculations of the Q factor for rectangular microwave resonators, where the power losses are divided into losses caused by the metallic walls that do not

reflect completely the electromagnetic waves and losses caused by the dielectric that is possibly present in the cavity. However for our two dimensional cavity (which will be described in section 2.6 of chapter 2) we assume that the main losses are caused by the apertures on the side of the cavity, whose power losses can not be easily evaluated. For the microwave resonators mentioned before the Q factor can assume values of the order of 10^6[27]. In the literature there are also experimental studies[28] on open microwave resonating cavities, which yields quality factors of the order of 10^3. Compared to those experiments, in our setup the Q factor is probably lower still, as the cavity walls are comparable in size to the wavelengths of the microwave radiation of interest. Therefore we estimate that for the final form of our cavity the Q factor is surely lower than 100, and maybe around 10. Further analysis, with the implementation of a simulation code of the modes spectrum of the cavity, could give us a more exact evaluation of the Q factor.

Chapter 2

Experimental setup

2.1 Introduction

My work carried out in the Rydberg laboratory in the Department of the Physics was mainly centred on the technical realization of the physical elements that we added to the apparatus. The basic idea was to create a 2D resonant electromagnetic cavity in the microwaves regime, exploit the cut-off frequency that would suppress BBR-induced transitions between Rydberg levels and therefore extend the lifetimes of the originally populated levels (see black body radiation deviation from Planck's formula (1.4.1) and Rydberg atom lifetimes (1.2.3)). During my thesis work I used experimental techniques such as the cooling and trapping process of Rubidium atoms with laser beams and an magnetic field, to get a system of almost stationary atoms (called *magneto-optical trap*, alias MOT), which can then be excited by other lasers. These techniques had been thoroughly studied in the laboratory before the beginning of my experiments.
I will describe exhaustively the additions I made on the system, which are fundamental for the results I deal with in the following chapter. The main addition in the first place consisted of metallic meshes which reflect almost completely electromagnetic microwaves but transmit light in the optical domain. These properties allowed us to create a microwave cavity by placing the metallic meshes around the glass cell so that the laser beams used for the cooling process could pass through the meshes without any significant loss of power, and in this without interfering with the MOT operation. Later Aluminium plates were placed around the glass cell in order to extend the walls of the cavity.

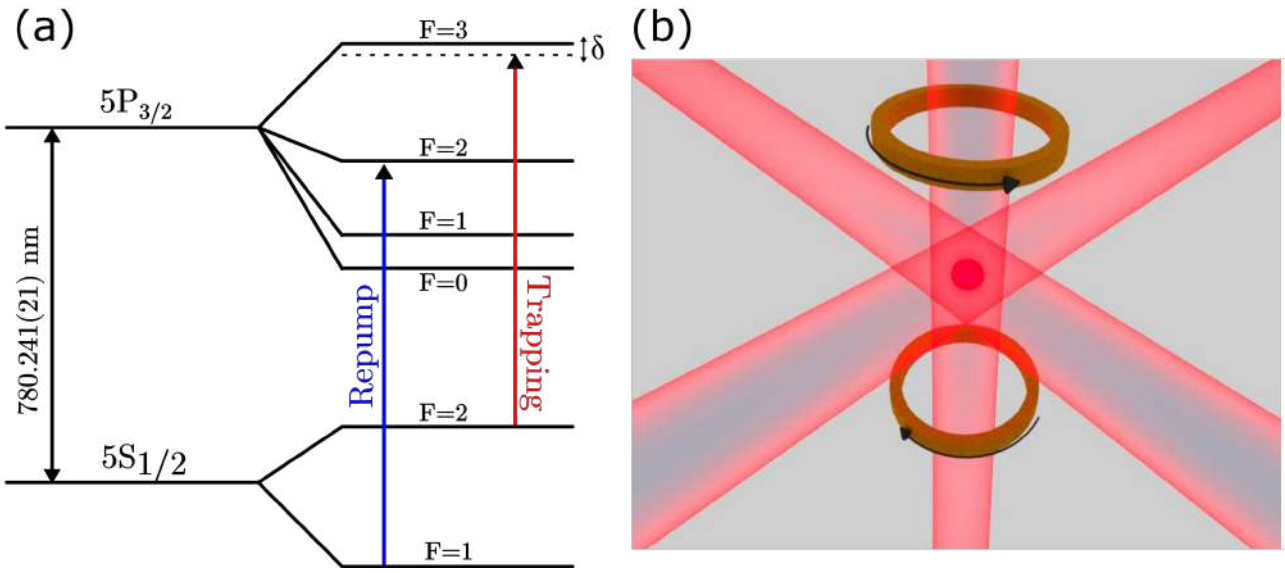

Figure 2.1: Scheme of the Rubidium levels with the transitions used by the cooling process (a). Scheme of the MOT apparatus with the counter-propagating laser beams and the magnetic coils (b).

2.2 The MOT setup

The main part of the apparatus consists of the *magneto-optical trap* (MOT), a typical atom cooling setup that exploits the interaction between laser light and atoms in the presence of a quadrupole magnetic field [29][30]. An accurate description of the apparatus can be found in [8]. The purpose of this process is to obtain from a gas of atoms at room temperature a particular region where some atoms are both concentrated and slowed down, i.e. a gas cooled down to low temperature, in order to operate on them with further lasers pulses.

The MOT uses the cooling effect induced by three pairs of counter-propagating laser beams, and a pair of magnetic coils in anti-Helmholtz configuration (Figure 2.1(b)), centred on a silica quartz cell held under vacuum pressure, containing Rubidium atoms (originating from a Rb dispenser inside the vacuum system). The coils produce a quadrupole field that causes a Zeeman effect on the atoms. This makes the recoil effect produced by the photon absorption process space dependent and the atoms are concentrated in the centre of the magnetic field, where the gradient of the field has its minimum.

In the laboratory I worked with ^{87}Rb Rubidium isotope. The transition used for the laser cooling (see the scheme of Figure 2.1(a)) is $|5^2S_{1/2}, F = 2\rangle \rightarrow |5^2P_{3/2}, F' = 3\rangle$. In the cooling cycle, it is possible that atoms decay to $|5^2S_{1/2}, F = 1\rangle$ instead of $|5^2S_{3/2}, F = 2\rangle$. In this case they would exit the cycle. Therefore, another laser is necessary, called repump laser, that is tuned to the transition $|5^2S_{1/2}, F = 1\rangle \rightarrow |5^2P_{3/2}, F' = 2\rangle$ and its beams are co-propagating together with the beams of

the first laser. In this way the atoms are brought back into the cycle.
With this setup, before my experiments, we got typical MOTs of 5×10^8 atoms in a volume of $200\,\mu\text{m} \times 200\,\mu\text{m} \times 300\,\mu\text{m}$, with an atom density that ranges between 10^{10} and $10^{11}\,\text{cm}^{-3}$. These values are obtained a CCD camera that is pointed on the atoms along the y axis (see Figure 2.3 for the axis orientation), that detects atoms by their fluorescence caused by the cooling cycle. The mean temperature of the atoms is about $150\,\mu\text{K}$, obtained by measuring the mean velocity of the atoms. The latter is measured by observing the ballistic expansion of the atoms after the trap lasers have been turned off, and corresponds to about $100\,\mu\text{m/ms}$. After the placement of the elements concerning my experiments the number of atoms trapped inside the MOT decreased as the intensity of the laser beams was reduced, but this did not adversely affect the measurements.

2.3 Excitation of Rydberg states

Once the MOT is formed, we proceed to excite Rydberg atoms. Several methods for exciting Rydberg states have been described in the literature [31][19][32][33]. In our laboratory we use photo-excitation with lasers, as it allows us to excite with precision the desired Rydberg level. This is because the linewidth of the laser used, of the order of few hundreds of kHz, is much smaller than the distance between the Rydberg levels we excite (of the order of GHz for the levels with principal quantum number between 65 and 110, used in this thesis). Moreover, we use a two photon excitation, instead of using a single photon one. Single photon excitation would give us access only to the P states because of the dipole selection rule (we start exciting from the $|5^2S_{1/2}, F = 2\rangle$) and it would force us to use an ultra-violet laser beam. Using two photons allows us to reach both S and D states.
The beam of the first laser is tuned close to the $|5S_{1/2}\rangle \rightarrow |6P_{3/2}\rangle$ transition. This light is produced by a Toptica TA-SGH Pro laser, which consists of a 842 nm diode laser injected into a tapered amplifier, whose beam is injected into a duplicating crystal that produces 421 nm blue light with a linewidth of $2\pi \times 400\,\text{kHz}$. This beam is focused on the atoms with a waist of $40\,\mu\text{m}$ and a maximum power of 1 mW. The other laser light is tuned close to the transition between the $|6P_{3/2}\rangle$ level and the desired Rydberg level. The light is produced by a Toptica DL100 external cavity 1012 nm diode laser with a typical output power of 20 mW and a frequency width of about $2\pi \times 400\,\text{kHz}$. Its output is injected into a tapered amplifier with a typical 150 mW output power. This beam is focused on the atoms with a waist of $90\,\mu\text{m}$ and maximum power of 15 mW, co-propagating with the blue laser.
Therefore, the excitation volume is a cylinder with a diameter of $40\,\mu\text{m}$, given by the 421 nm laser, and $200\,\mu\text{m}$ length given by the size of the MOT, which equals to a volume of $10^{-3}\,mm^{-3}$.
Each laser beam passes through an Acousto-optic modulator (AOM), an optical device that applies a moving diffraction grating on the incident beam once it is activated by a TTL pulse. The diffraction

causes a frequency shift on the laser light if a non-zeroth order is used after the AOM. In this way the laser beams that arrive on the atoms can be switched on and off with the time delay of the AOM activation, that is about 100 ns. AOMs are also used to switch off the trap laser beams during the Rydberg excitation.

Rydberg atoms are excited with two simultaneous laser pulses, which are applied a few μs after

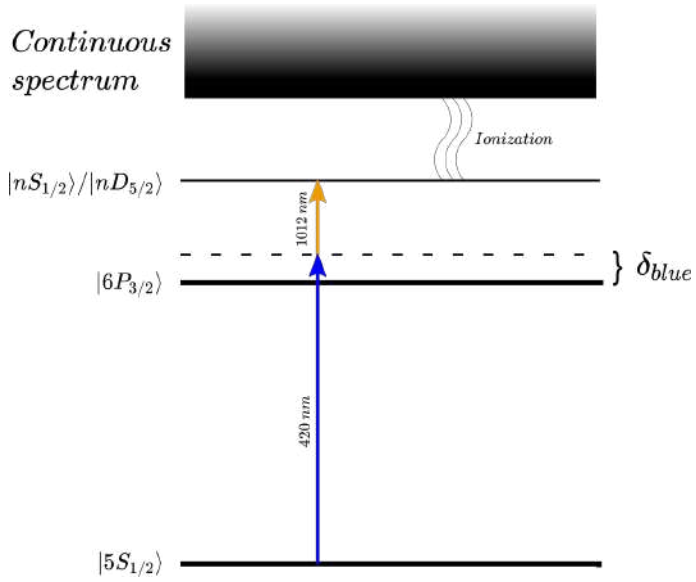

Figure 2.2: Scheme of the two-photon excitation scheme and the following ionization of a Rubidium atom. Figure adapted from [8].

the MOT trap laser beams are turned off. This delay is chosen such as to be sure that there are no atoms in the $|5^2P_{3/2}, F' = 3\rangle$ state, which otherwise could be ionized by the following 421 nm pulse. The 421 nm pulse is blue-detuned from the $|5S_{1/2}\rangle \rightarrow |6P_{3/2}\rangle$ resonance in order to avoid the population of the$|6P_{3/2}\rangle$ level, but still close enough to ensure a sufficiently large two-photon Rabi frequency, and hence a large enough two-photon excitation rate. The laser at 1012 nm is tuned close to the resonance of $|6P_{3/2}\rangle \rightarrow |nS_{1/2}\rangle$ transition or $|6P_{3/2}\rangle \rightarrow |nD_{5/2}\rangle$ (Figure 2.2). For the experiments shown in this thesis we usually used an incidence power of 0.25 mW for the blue laser and 18 mW for the IR laser. These powers with pulses of about 500 ns are sufficient to produce the necessary number of Rydberg atoms that are detected with our ionization technique. How many atoms are excited will be explained in the following chapter concerning Rydberg lifetimes measurement technique (3.2).

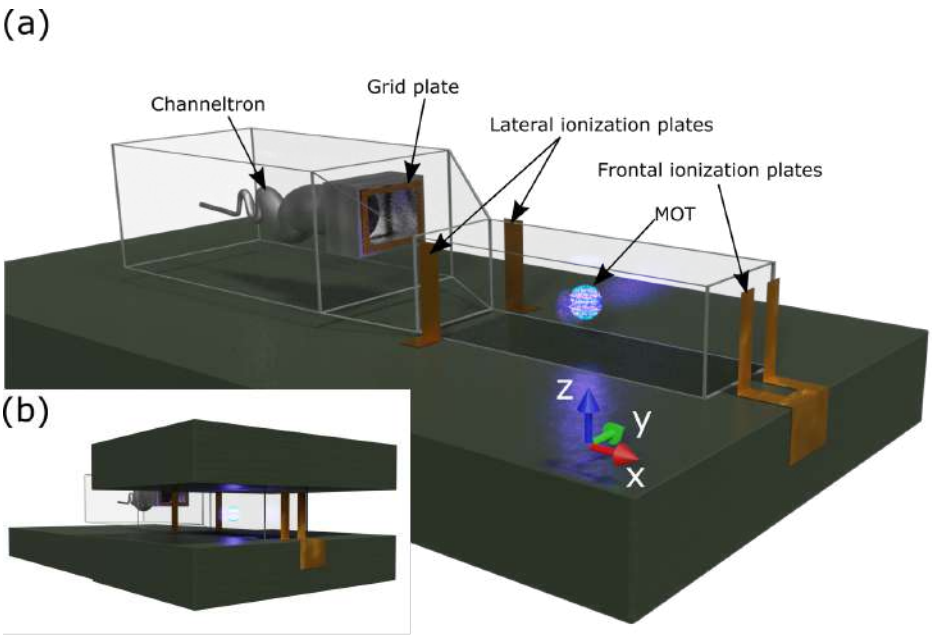

Figure 2.3: 3D model showing the positions of the ionization plates and the Channeltron in relation to the cell and the MOT (a), and position of the plastic support (b).

2.4 Ionization and detection

Once the atoms have been excited to Rydberg states, we can detect them by ionizing them with a brief electric field pulse. This electric field is created by two sets of copper plates placed around the silica quartz cell. One set, called *frontal plates*, is placed along the x axis and the other, called *lateral plates*, along the y axis (see Figure 2.3(a)). These plates produce an electric field at the position of the MOT strong enough to overcome the Rydberg levels ionization threshold for states with $n > 70$ ($E_{ion}(70S) = 16.25\,\mathrm{V/cm}$ for instance).

Right after the ionization, the field pulse also accelerates the ions just created towards the aperture of a Channeltron electron multiplier. The Channeltron is placed on the x axis of the cell, on the opposite side of where the excitation beam arrives, and a little higher than the cell in order not to block the laser beams (Figure 2.3(a)). In front of its aperture there is a rectangular electrode, on which at the same time of the other plates a negative voltage is applied to accelerate the ions towards the Channeltron where they arrive $13\,\mu$s after the ionization pulse. Once inside the Channeltron channel, the ions charge is multiplied and we detect the ions as voltage peaks on an oscilloscope. The voltage pulse on the frontal and lateral plates has a typical duration of $7\,\mu$s, while on the grid it lasts about $30\,\mu$s.

Each voltage pulse is controlled by a TTL pulse sent to three high voltage switches, connected to the frontal plates, the lateral plates and the rectangular electrode. The delay time between these TTL pulses and the TTL pulses of the excitation pulses is adjusted according to the desired wait time.
The overall detection efficiency of this procedure is about 40% [34], in the following experimental data, the numbers of Rydberg excitations reported have been corrected for this efficiency.

2.4.1 Adjustment of the ionization and detection

Regarding the ionization and detection of Rydberg atoms during the experiments with the resonant cavity (see the following sections), adding this element to the setup complicated both processes. In fact, we observed that the presence of the new elements changed drastically the electric field lines inside the cell. This meant that the ions produced did not accelerate properly towards the Channeltron aperture, and so our detection efficiency was reduced to zero. However, I managed to restore the usual detection efficiency by changing the voltage applied on the lateral plates for each configuration of the elements of the resonant cavity[1]. In this way, we were sure that we were exciting similar numbers of atoms during our measurements.
Moreover each element of the cavity had to be connected electrically to the ground, since if the elements were left on a floating potentials, the field inside the cell would not have remained stable and caused fluctuations on the detection efficiency.

2.5 Field compensation

We observed [8][9] from measuring directly the Rydberg Stark shift that in the region occupied by the MOT there is an electric background field of about 200 mV/cm. We speculated about the source of the field: the Rubidium deposited on the internal walls of the cell could mainly contribute to this field, or also small specks of dust resting on the surface of the cell. Such dust particles can carry several thousands of elementary charges[35], which translates into an electric field at the position of the MOT comparable with the observed background field. As I explain in the theoretical section regarding the Stark shift of Rydberg levels (1.2.1), the magnitude of the field is high enough to mix the nL Rydberg levels we are interested in with the $l > 3$ levels manifold. As we have shown in a previous work [15], the lifetimes mixed levels are much shorter than the non-mixed ones (by up to two orders of magnitude). Therefore it is necessary to compensate this field using an

[1]The detection efficiency was checked by measuring the numbers of ions detected with specific settings of powers and pulse duration of the excitation lasers. We compared this value with the one obtained before the placement of the cavity elements and ensured that it was similar, scaling the two numbers accordingly to the dimensions of the MOT.

external applied electric field. The electric field required for this compensation is produced with three sets of electrodes, one for each Cartesian axis. The electrodes concerning the x and y axes were initially brass electrodes placed around the cell, while along the x axis the compensation field is always applied with the frontal plates used also for the ionization and detection. The voltage on the latter is changed from the compensation value to the ionization one with the high voltage switch. During the experiments on the modification of the BBR, the brass electrodes were replaced by other elements described in the following sections. The voltage on the electrodes is applied just before the excitation pulse and kept for about 1.5 ms on the y and z axes until the field ionization pulse is sent on the atoms. This time interval allows us to apply the desired laser pulses tuned on the Rydberg levels with the electric field compensated during the lifetimes measurements, which usually were shorter than the duration of the compensation pulse. The voltage pulse is controlled by three opto-couplers, one for each pair of electrodes (where one electrode of each pair is connected to ground).

There are two ways to determine the correct voltages to compensate the electric field. The first one is to find a Rydberg state resonance, change the voltage of one of the sets of electrodes and see whether the Rydberg energy level rises or falls according to the Stark shift (see Stark shift section (1.2.1)). The field minimum along that direction is determined by the voltage value for which the Rydberg energy level is highest. Iterating this operation with each set of electrodes allows us to bring the electric field to its minimum.

Another method consists in setting the 1012 nm laser frequency on the edge of a Rydberg manifold and minimize the Stark shift by reducing the number of Rydberg atoms detected, hence bringing the lasers out of resonance with the manifold (see Figure 1.1 in the Stark shift section (1.2.1)). This operation is done on each set of electrodes, as in the first method.

By using these methods, it is possible to reduce the magnitude of the residual background field to about 15 mV/cm.

2.6 Modification of the BBR

In our work on Rydberg state lifetimes we found deviations from the theoretical lifetimes that we attributed to deviations from Planck's formula, induced mainly by the geometry of the silica quartz cell [15]. On the basis of this interpretation, we hypothesized that it should be possible not only to increase the BBR-induced transitions in certain frequency ranges, but also suppress them (see section (1.4.1) and section (3.6.1) for the model of the density of modes we developed).

In this section, I focus on the crafting and placement of the elements that have been used to modify our the BBR spectrum.

2.6.1 Geometry of the cell surroundings

For the understanding of the following sections, it is necessary to properly understand the geometry of the apparatus as it was before the beginning of my experiments.
The MOT is produced at the centre of a fused silica (Vycor) cell with a parallelepiped shape, with external dimensions of $30 \times 24 \times 90$ cm and internal dimensions of $24 \times 18 \times 87$ cm. The excitation beams arrive on the MOT passing through the frontal ionization plates shown in Figure 2.3(a). While on the side where the aperture of the Channeltron is placed the cell is connected to the rest of the vacuum system with a graphite tube, through which Rubidium atoms are pushed inside the cell via an additional laser beam. The cell is placed between two plastic supports that keep the cell protected and sustain the quadrupole field coils (Figure 2.3(b)). The horizontal counterpropagating lasers pass in between the two plastic supports, while the vertical ones pass through the apertures of the magnetic coils (which are not shown in the model).

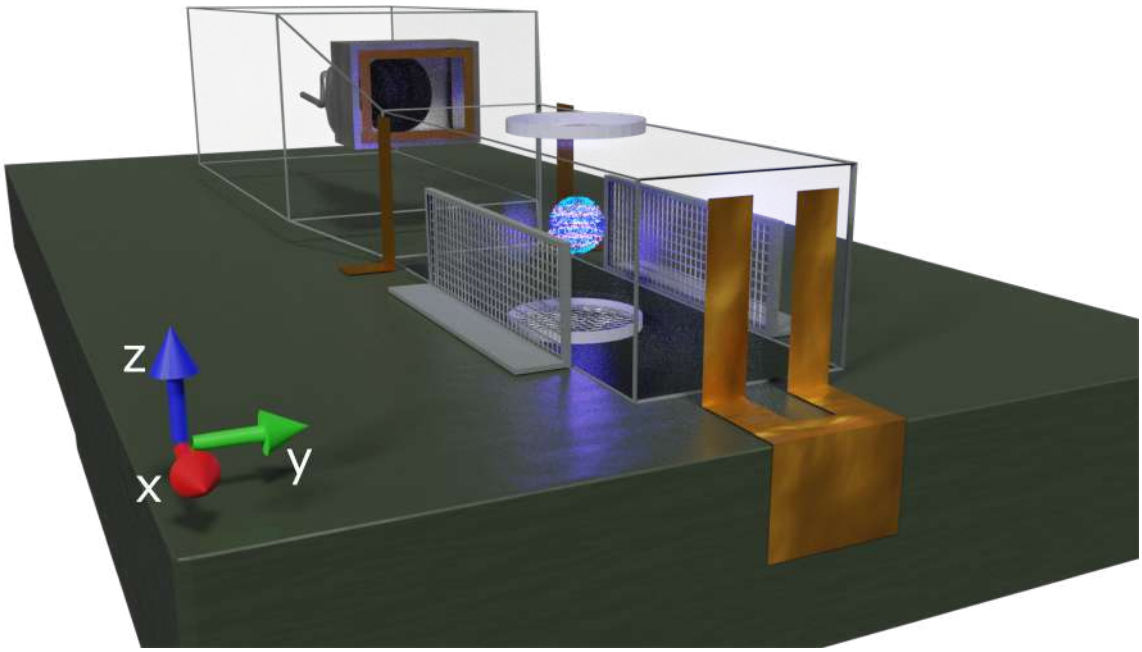

Figure 2.4: A 3D model of the apparatus including the two pairs of meshes.

2.6.2 Meshes

Initially, the project consisted in placing metallic meshes with their surfaces parallel to the x direction to form a two dimensional cavity extended on the y-z-plane, as it is shown in Figure 2.4. While the extension of the cavity along the x axis was impossible, as one of the walls should have been placed inside the vacuum system. The BBR-induced transitions of the Rydberg states that we

are able to excite cover a range from about 3 GHz to 10 GHz. This means that the cavity lengths must stay between about 1.5 cm and 5 cm to have its fundamental modes within that frequency range. In fact, our expectation was to place the frequency cut-off of the cavity in a way that the BBR-induced transitions with lower frequencies than the cut-off one would be suppressed. Therefore lifetimes of Rydberg states with those transitions would have been extended.
We implemented the mesh supports so that it was possible to adjust the two lengths of the cavity and, moreover, to apply a fixed voltage on each mesh. This allowed us to use them as electrodes to compensate the field at the position of the MOT instead of using the previous electrodes, which had to be removed in order to place the meshes.
we used steel mesh *50 Mesh T316 Stainless High Transparency .0012" Wire Dia* that is produced by *TWP*. the mesh has a rectangular shape and its wires are 30.5 μm thick and the apertures are 480 μm wide, much smaller than the wavelength of the cavity we want to create.
A test has been performed on the mesh reflectivity for the 780 nm trap laser beam as a function of

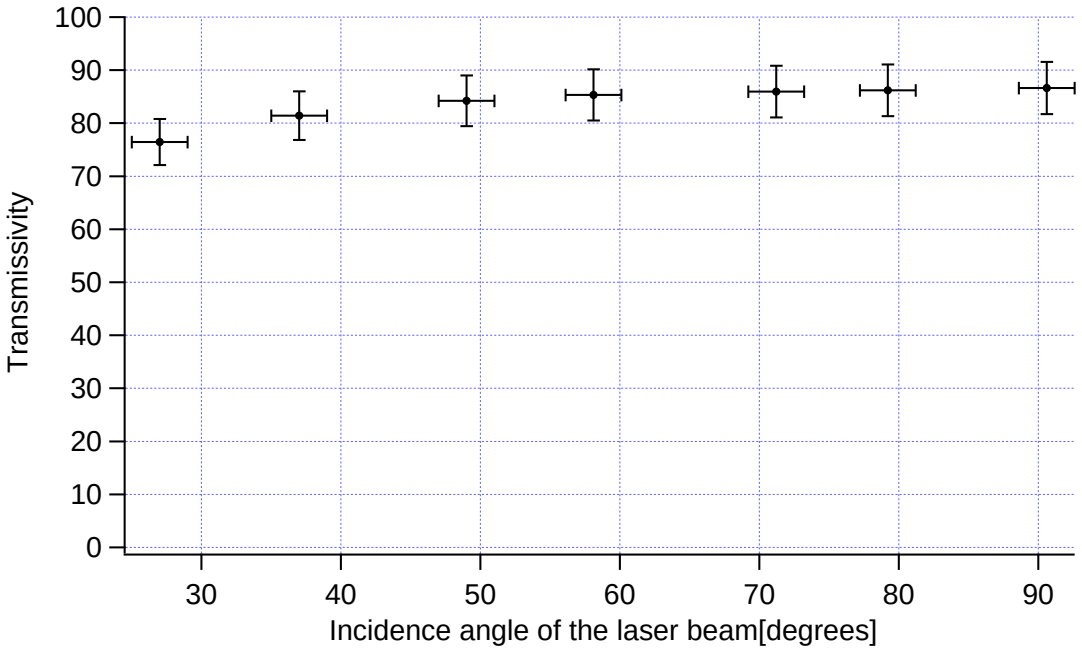

Figure 2.5: Mesh transmissivity as a function of the incidence angle of the 780 nm laser beam. Incidence power equalled to 46.3 mW.

the incidence angle (Figure 2.5), resulting in minimum transmissivity of 75%. This transmissivity allowed the horizontal trap beams in out MOT setup to pass without significant loss of power, with a ~ 45 degree angle. Moreover, a qualitative test on the reflectivity of the mesh in the microwaves ranges was performed with a microwave generator connected to an antenna and an electromagnetic spectrum analyzer. The results shown a minimum reflectivity of 90% with a 3 GHz microwave.

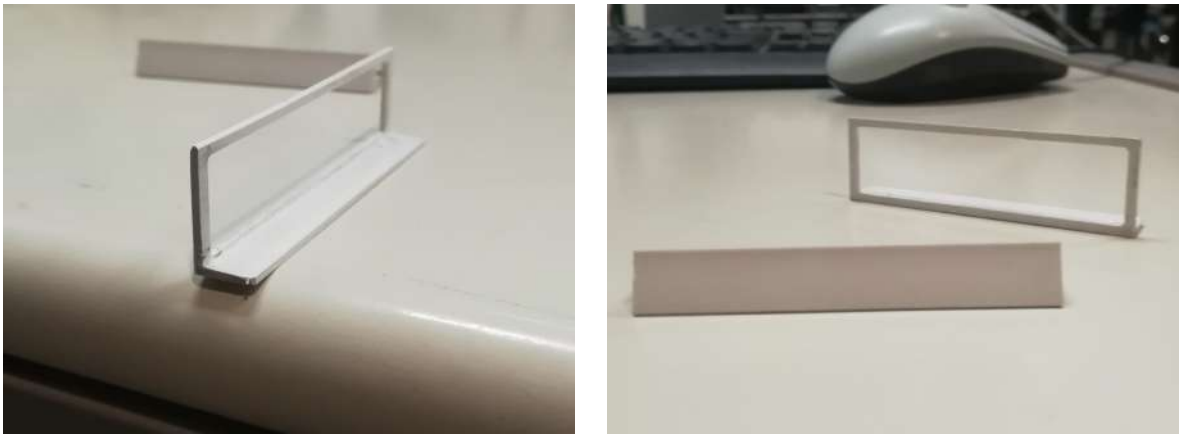

Figure 2.6: Two photos of the plastic supports for the vertical meshes that act as walls along the y dimension.

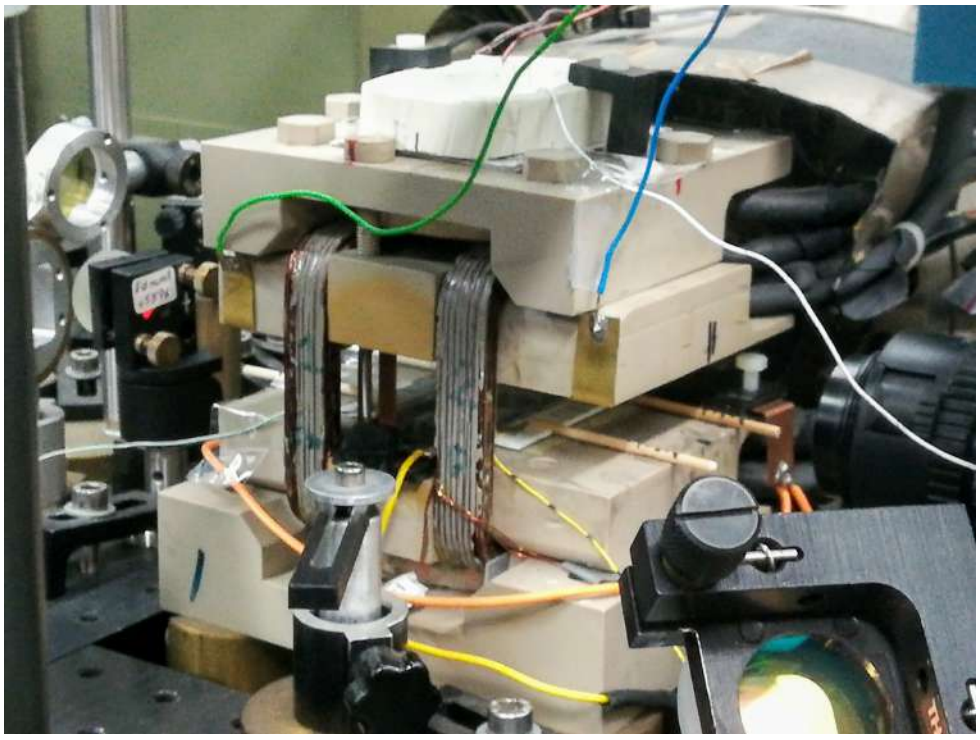

Figure 2.7: Photo of the two pairs of meshes that acted as vertical walls of the resonant cavity placed beside the cell with pairs of wooden sticks connected to each support of the meshes. Those sticks helped to place the pair parallel to each other and at the desired distance, with a precision of 2 mm

Figure 2.8: On the left side, a close-up photo of the bottom mesh seen between the frontal ionization plates and through the cell (The Aluminium plates mentioned in section (2.6.3) are already placed). On the right side, a photo of the upper part of the tube that sustains the top mesh. Note the ticks that allowed us to adjust the distance between the upper mesh and the cell with a precision of about 1 mm.

The vertical walls of the cavity were created by attaching two rectangular pieces of the mesh on a pair of plastic frames, with a base allowing to place them on the cell plastic support (Figure 2.6). We designed these frames to be as large as possible to prevent them from blocking the MOT beams, which arrive on the cell with a waist of 8 mm, however the elements of the apparatus that surrounds the cell limited the width and the height of the mesh supports. In fact, the height of the supports was limited by the distance between the two plastic supports. While the width of the supports was limited by geometry restrictions on the aperture of the cell, and on the other side by the position of the lateral ionization plates. In the end, we crafted the frames to be 6×1.8 cm large. Initially, we attached the meshes only at the centre of the frames with a width of 1.5 cm, to let the MOT beams pass in between the meshes. To electrically connect the meshes, we used a two-component glue with silver to connect the meshes to electric wires.

Regarding the horizontal walls of the cavity, we crafted two cardboard pipes of the central aperture inside the MOT coils. At one end of each pipe were attached circularly shaped pieces of mesh with a diameter of 21 mm just to fit inside the coils. We glued a circular buffer over the mesh to put them as close as possible to the silica quartz cell without damaging its surface. Finally, electric wires were bound to the meshes and connected to the inner tubes surface to connect electrically the meshes to a fixed voltage, without blocking the trap laser.
The horizontal meshes were placed in apertures the coils above and below the cell. The bottom tube was placed with a fixed distance between the mesh and cell surface of about 2 mm, exploiting as support for the tube a wave plate (left side of Figure 2.8). As regards the top mesh, we suspended

its tube through the coil aperture, inserting it in a cardboard provided with a fitting hole, and fixing the cardboard on the top of the plastic support (right side of Figure 2.8). In this way we were able to adjust the distance between the mesh and the cell by pushing in or pulling out the pipe from the cardboard.

With this arrangement, shown in Figure 2.9, we were able to adjust the horizontal dimension of

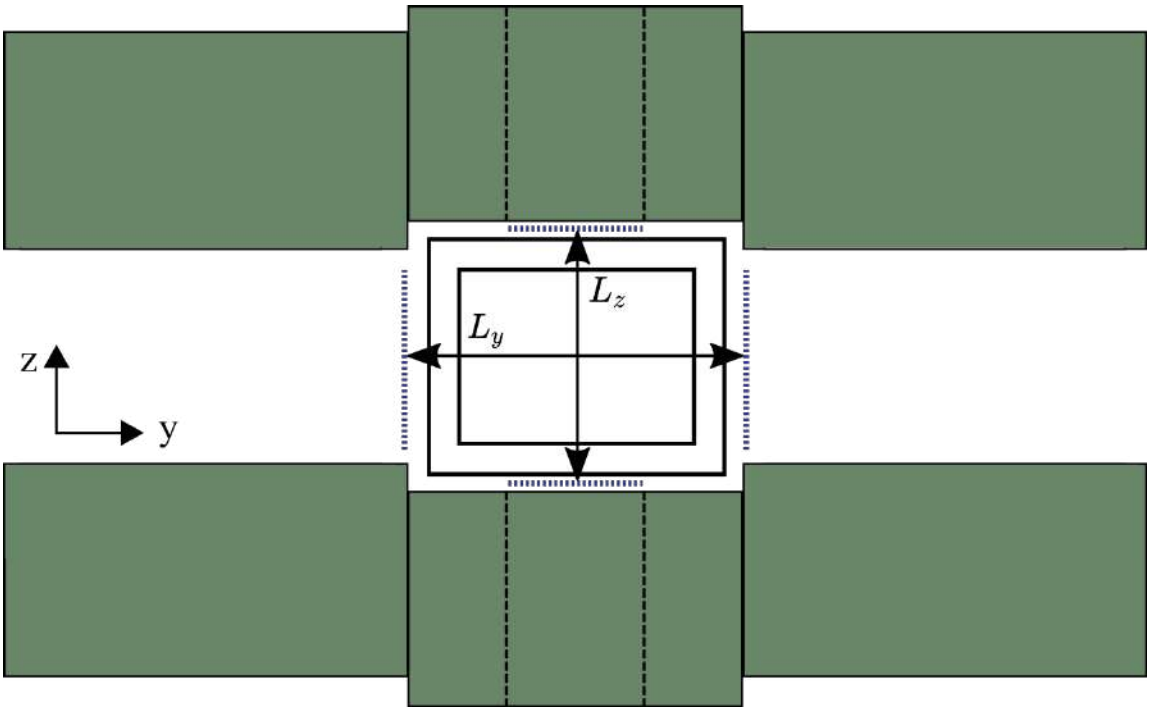

Figure 2.9: A section of the surrounding of the silica cell along the y-z-plane, showing the position of the two pairs of meshes.L_y and L_z are the dimensions of the two dimensional resonant cavity.

the cavity (L_y) in a range of 30-46 mm, that equals to a range of the fundamental harmonic from 3.3 to 5 GHz, whereas with the vertical dimension (L_z) we were able to cover the length range of 26-34 mm, i.e. the frequency range of 4.4 to 5.8 GHz (see BBR resonant cavity section (1.4.1)). However, the frequency ranges mentioned before were calculated without taking into account the presence of the cell inside the resonant cavity. I will discuss the expected modifications of the resonant frequencies in the following chapter regarding the experimental results (3.6.1).

In the end, we had to make some considerations for the configuration of the cavity. Firstly, we have to take into account that in our cases we do not have an ideal closed cavity, but clearly an open one. Moreover, the extension of the walls are comparable with the wavelengths ranged by the cavity. These two considerations lead us to estimate that the Q factor of the cavity is quite low, as the energy losses of the cavity can be significant (a more in-depth analysis of the quality factor of the cavity can be found in section 1.4.2)). With the configuration just explained, we

performed experiments with different lengths of the two dimensions of the cavity. After that, as we improved the MOT formation system meanwhile and increased its trapping efficiency[2], we decided to continue with the lifetimes measurement extending the vertical mesh on the overall surface of the frame that sustained them. In this way transmissivity for the trap laser was reduced, but we were still able to form the MOT. The results of these last measurements are shown in section 3.6.2 of the experimental results chapter.

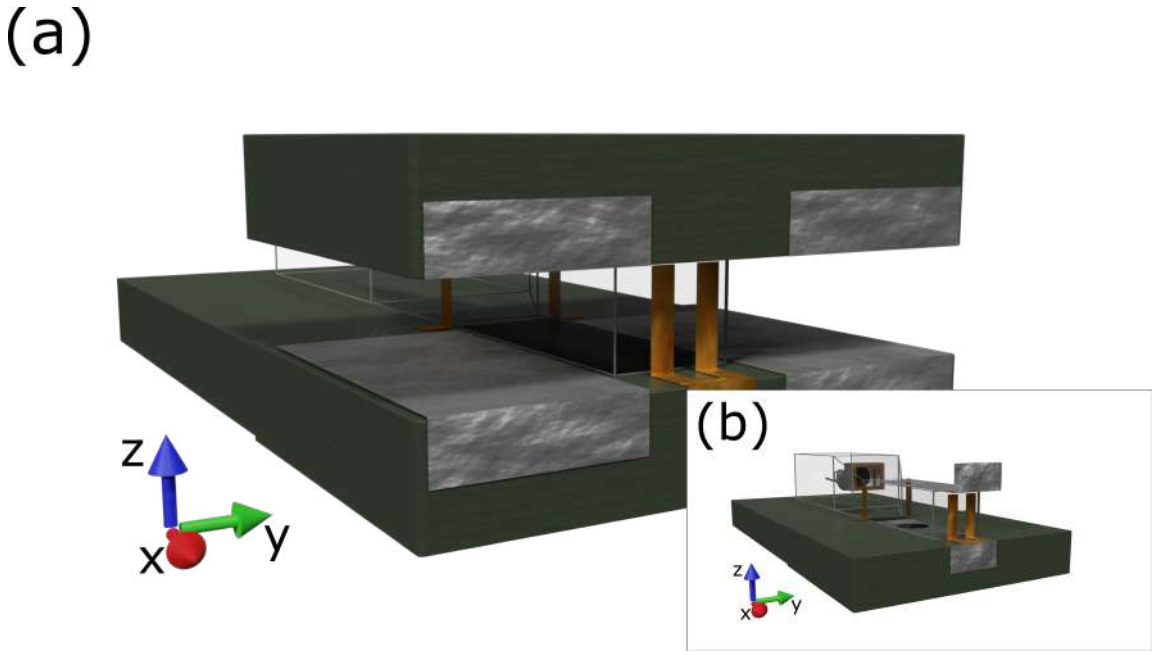

Figure 2.10: Two 3D models showing the placement of the Aluminium plates on the side of the cell (a) and on the top and the bottom of the cell (b).

2.6.3 Aluminium plates

After the experiments with the mesh, decided to try to further increase the Q factor of the cavity by extending its horizontal walls, exploiting the presence of the plastic support (see the model of Figure 2.3(b)) above and below the cell. We covered the inner surfaces of this support with Aluminium plates on their internal surfaces, to the side of the cell (Figure 2.10(a)). The Aluminium plates, being metallic, reflect the microwaves and act as part of the horizontal walls of the cavity. The

[2]During the experiments we found that the detuning of the trap laser frequency was set on a non-optimal value. After changing the detuning, we observed an increase of the numbers of atoms by a factor of 3.

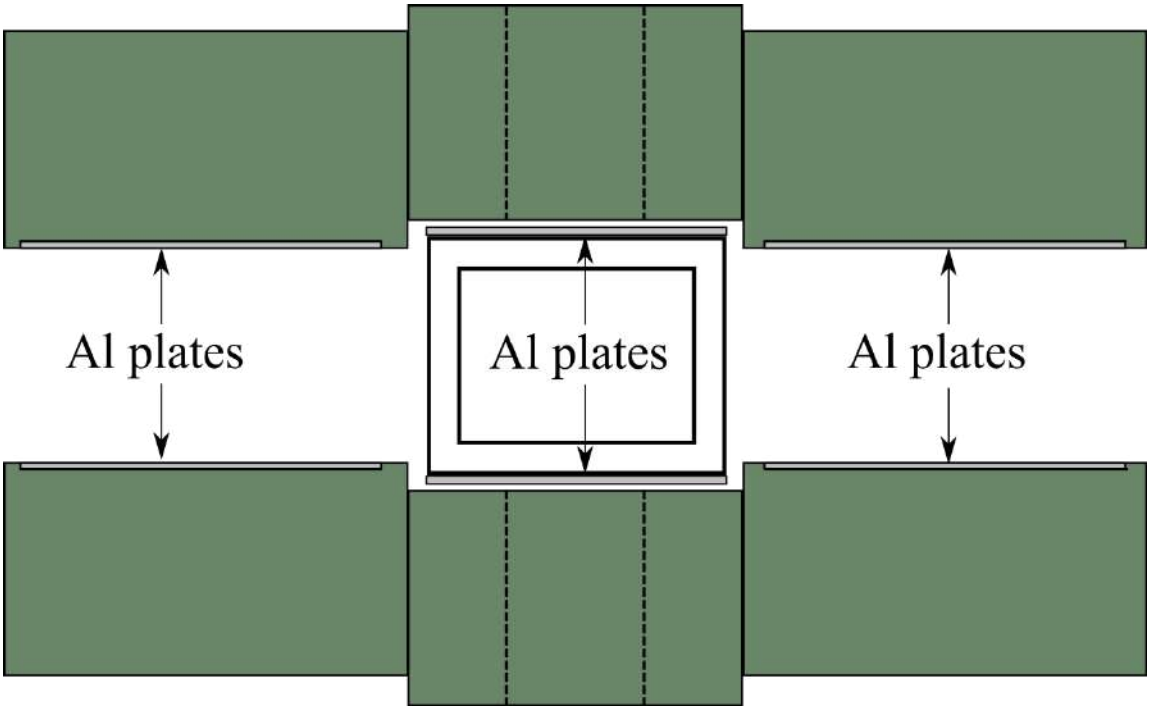

Figure 2.11: Section of the cell and the plastic support on the y-z-plane with realistic proportion, with the presence of the Aluminium plates on the side of the cell and the ones above and below the cell. The dotted lines show the positions of the tubes of the vertical meshes.

plates had a rectangular shape with a size of 4×6 cm, covering all the accessible surface. In this way we extended the horizontal walls, formed by the horizontal mesh and the Aluminium plates, to a width of about 11.8 cm.

After these changes of the apparatus, the vertical walls of the cavity have a complex the geometry that can be seen in Figure 2.11. The Aluminium plates on the side of the cell are at a distance of 21 mm, while closer than the vertical mesh (against about 26 mm). So the plates can actually be considered as walls of a secondary external cavity. This results in an overall more complex frequency spectrum than the one of a cavity with simple flat walls.

With the last configuration I measured a set of Rydberg lifetimes. After that, we placed another pair of Aluminium plates right above and below the cell, covering partially the two cell surfaces (see Figure 2.10(b)), with a size of 90×30 cm. These Aluminium plates had the purpose of matching the other Aluminium plates in order to obtain smoother horizontal cavity walls and so to improve even more the quality factor (see the scheme of Figure 2.11). With this last addition, I performed experiments with different lengths of the horizontal dimension of the cavity. For those experiments we left the horizontal meshes at the same distance as the Aluminium plates above and below the cell. The results of these measurements can be seen in section 3.6.3.

2.6.4 Adjustment of the compensation system

The two pairs of meshes were used for the field compensation (2.5) along the y and z axes, replacing the metallic electrodes that were already present in the apparatus. All Aluminium plates were always connected to ground, except for a set of measures taken without the presence of the lateral meshes. In this case the two Aluminium plates on both sides of the cell were connected to the compensating potential.

In the following chapter I will discuss how the addition of the various plates and meshes described in this chapter affected the Rydberg state lifetimes.

Chapter 3

Experimental results

3.1 Introduction

In this chapter I will show the experimental data I obtained during my experiments, and the analysis I conducted on them.
Initially I will explain the lifetime measurement technique and the methods for calculating BBR rates. I will show the experimental results that were obtained with S and P Rydberg states before my experiments. These measurements yielded significant deviations between the experimental values and the theoretical ones. We hypothesize that these deviations were caused by deviations of the black body radiation from Planck's expression. I will show the measurements I performed on Rydberg D states to confirm these deviations of these state lifetimes and compare them to the S and P lifetimes measured before my experiments.
Lastly, I will show the experimental results obtained by measuring S state lifetimes after the creation of a microwaves resonant cavity (section 2.6) with the additions shown in the previous chapter. Different measurements were taken while changing the dimensions of the cavity, which influenced the mode density in the microwaves range. During the experiments, we create a model of the frequency spectrum that could predict the density of modes for the different configurations of the cavity.

3.2 Lifetime measurement

The lifetime measurements are conducted with a specific sequence of excitation, de-excitation and ionization pulses [15]. Once a set of Rydberg atoms are excited with the two photons laser pulse on the Rydberg state resonance (see section 2.3), the decay of those Rydberg atoms is governed by the black body radiation rate and the spontaneous rate (section (1.2.3)). We call *target* the nS or nD

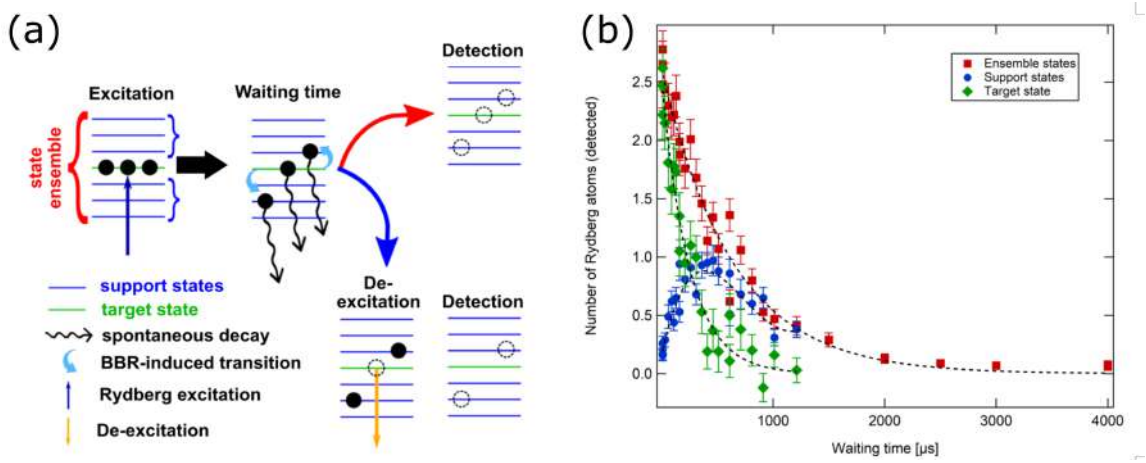

Figure 3.1: (a) Schematic of the lifetime measurement, taken from [15]. (b) Example of a Rydberg state lifetime measurement ($86S$).

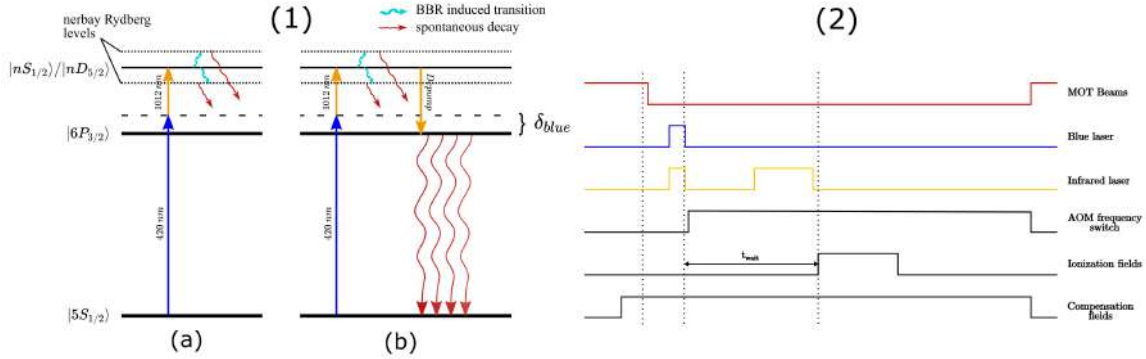

Figure 3.2: (1) Excitation schemes of the laser impulses used in the lifetime measurement: (a) Ensemble pulse and (b) support pulse. (2) chronological impulse scheme of the support measurement. Both figures are adapted from [10].

state initially excited. The black body radiation induces transitions to other Rydberg states with $n'L$ close to the one of target state, while the spontaneous decay rate governs the transition to low lying Rubidium states (around 95% of the atoms decay to states with n between 5 and 17). If the field ionization pulse is sent after a time t_{wait}, this ionization measurement yields the population of atoms that have not decayed to low-lying states yet. This population includes the atoms in the target state, as well as the atoms that have undergone a BBR-induced transition to neighbouring states and are still detectable by our system (in our experiments, the detection limit is around n=60). We called this set of states *ensemble* (see the schematic in Figure 3.1).
In order to measure exactly the target lifetime, we perform at different t_{wait} two routines of excitation and ionization (Figure 3.2(a)):

1) Rydberg atoms are excited and after t_{wait} they are ionized. Before the ionization, with a 1013 nm laser pulse close to the resonance with $|nRyd\rangle \rightarrow |6P_{3/2}\rangle$, the target state is de-excited, since atoms in $|6P_{3/2}\rangle$ decay spontaneously in less than 1 μs. The frequency switch between the excitation pulse and the de-excitation pulse of the 1013 nm laser is done by changing the radio frequency sent to the AOM through which the 1013 nm beam goes. We call the second pulse *depumping*, and it lasts 5 μs. The duration of the depumping process is chosen to be much shorter than the expected target lifetime, but long enough to de-excite most of the atoms in the target state. Those de-excited atoms no longer contribute to the ionization signal. The Rydberg state population that is measured in this case is called *support* (Figure 3.2(b)).

2) Same procedure as before, but the 1013 nm laser pulse is sent on the atoms off resonance, i.e. without changing the AOM radio frequency. Therefore this laser pulse doesn't affect the Rydberg population. Thus, the ensemble population is measured.

The excitation pulse is adjusted to last typically between 300 ns to 1000 ns and its Rabi frequency is chosen such as to excite about ≈ 2 Rydberg atoms (corrected for the detection efficiency). A smaller number of excited atoms would lead to an insufficient signal-to-noise ratio and would not allow us to measure with enough signal the overall Rydberg decay, while more atoms could cause unwanted effects such as dipole-blockade[6] or Penning ionization[36].
The relation for the routine without depumping is $N(t) = N_{ens}(t) = N_{tar}(t) + N_{supp}(t)$, while for the one with de-excitation is $N'(t) = N_{supp} = (1-\alpha)N_{tar}(t) + N_{supp}(t)$, where α is the depumping efficiency. So if we subtract the two equations, we get

$$N_{tar}(t) = \frac{1}{\alpha}(N(t) - N'(t)). \tag{3.1}$$

Performing a fit on this function with $N^*(t) = Ae^{-\frac{t}{\tau}}$, we get the target lifetime (τ_{tar}). We proved that the target state lifetime obtained by that fit is not influenced by the depumping efficiency if this efficiency is greater than 80%. We measure the ensemble lifetime (τ_{ens}), also performing a negative exponential fit.

3.3 BBR rates calculation

As we attributed the discrepancy between the experimentally measured and the theoretical lifetimes to deviations from the usual Planck's BBR spectrum, it is fundamental to get the BBR rates from the lifetime measurements. We developed two methods to calculate the BBR rates, and proved that the results are comparable for the measurements taken before my experiments with the resonant cavity.

3.3.1 Support method

This method has the advantage that it uses only experimental data and it doesn't need any theoretical input, although some approximations are needed. Let's start with the population equation for the support states:

$$\frac{dN_{supp}(t)}{dt} = -\Gamma_{spon} N_{supp}(t) + \Gamma_{BBR} N_{tar}(t) \tag{3.2}$$

Now lifetimes measured in our experiments ranged between 100 μs and 300 μs. So if we consider the first 100 μs of the population evolution, the first term at right-side of the equation is negligible, as most of the atoms are still in the target state. Moreover, for the lifetimes mentioned before, the number of atoms in the target state can be considered constant, thus $N_{tar}(t) \simeq N_{tar}(t=0)$. Therefore, the support population in the first times of evolution is:

$$N_{supp}(t) = \Gamma_{BBR} N_{tar}(t=0)t + N_{supp}(t=0) \tag{3.3}$$

Finally if we perform a linear fit over the first 100 μs on the support evolution with a function of the form $N_{supp}^{fit}(t) = at + b$, we have that $\Gamma_{BBR} = \frac{a}{N_{tar}}$.

3.3.2 Target method

This other method uses both experimental and theoretical data. Once we obtain the target lifetime, we know that

$$\frac{1}{\tau_{tar}} = \Gamma_{tot} = \Gamma_{BBR} + \Gamma_{spon}. \tag{3.4}$$

So if we subtract from Γ_{tot} the theoretical spontaneous rates, that are obtained with ARC, we obtain again the BBR rates.

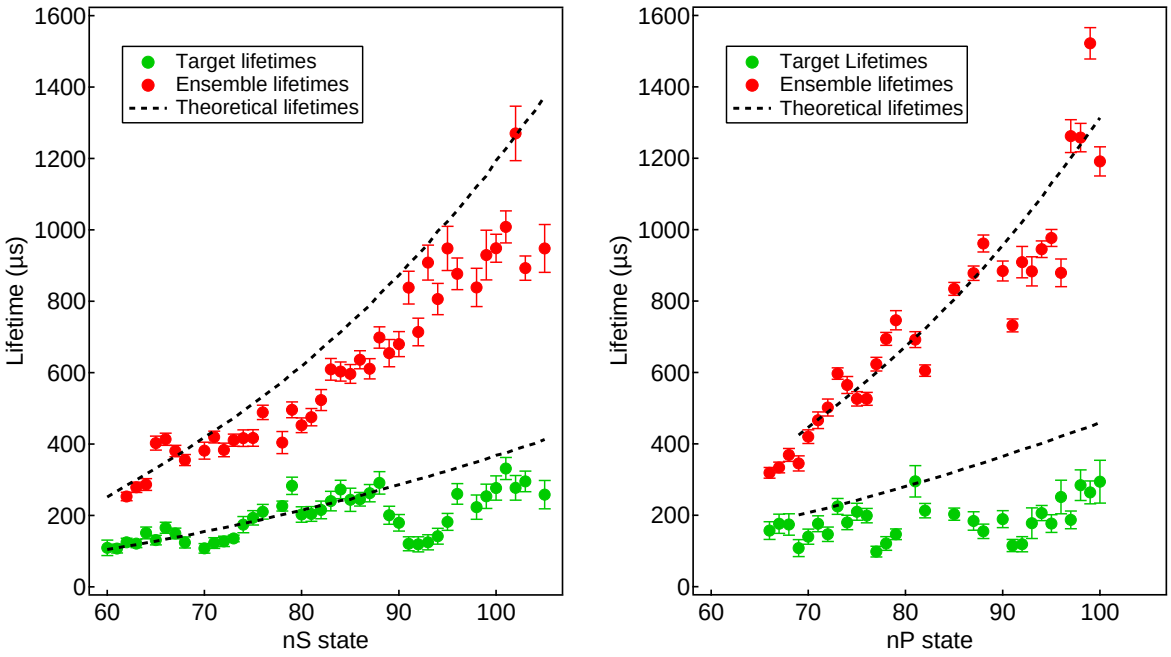

Figure 3.3: Target and ensemble lifetimes (respectively in green and red) of the S (left-side) and P states (right-side), compared to their respective theoretical values (black dashed lines).

3.4 S and P measurement

In Figure 3.3 the lifetime measurements of S and P states are shown. This data were taken before the beginning of my experiments. Part of the S lifetimes were published in [15]. As can be seen from the S state lifetimes, the data regarding the ensemble lifetimes shows a good agreement with the theoretical lifetimes. The target lifetimes measures, on the other hand, show significant deviations, mainly localized around nS states with n about from 90 to 95 and n from 68 to 72. The fact that these deviations regard only target states led us to the hypothesis that these deviations are caused by deviations of only BBR rates. To prove this hypothesis we calculated the BBR rates with the two methods just explained (Figure 3.4). Regarding the S states, the two methods gave us BBR rates that agree with each other to within their errors bars. By contrast, for the P states significant differences can be noted, since, for most of the states, the difference between the two values is larger than the errors bars. Moreover, the trends of two set of BBR rates appear not correlated. We attributed these differences to the depumping efficiency, which for most of the measurement was lower than 90% and may have distorted the BBR rates calculation with the support method. We developed a calculation that reduced these differences.

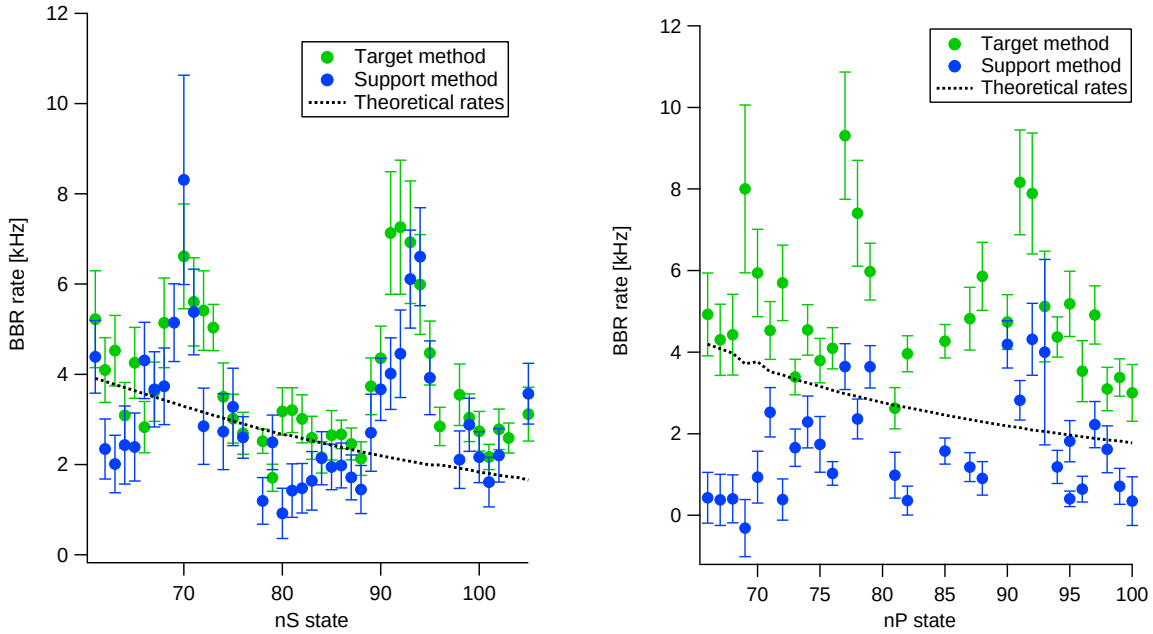

Figure 3.4: BBR rates of the Rydberg S (left-side) and P (right-side) states. In green the BBR rates calculated with the target method, in blue the ones calculated with the support method. The experimental rates are compared to the theoretical ones (black dashed line).

3.4.1 Correction for low depumping efficiency

In the lifetime measurement section, we saw that the number of atoms detected with the support routine are:

$$N' = (1-\alpha)N_{tar}(t) + N_{supp}(t) \tag{3.5}$$

where the depumping efficiency is defined as $\alpha = 1 - N'/N$. Hence if $\alpha = 1$, we have actually $N' = N_{supp}(t)$. But for lower α, this is not true anymore. To implement a correction we consider the time derivative of (3.5):

$$\frac{dN'}{dt} = (1-\alpha)\frac{dN_{tar}}{dt} + \frac{dN_{supp}}{dt} \tag{3.6}$$

Also here we have that if we have a good depumping efficiency the derivative of N' and N_{supp} are equal, and performing the linear fit in the first $100\,\mu$s of $N'(t)$ we actually get $\frac{dN_{supp}}{dt}$. But for low α we must take into account the first term of the left-hand side of (3.6).

From Equation (3.1) we get the relation between $N_{targ}(t)$ and $(N - N')(t)$. As said before, we

perform a fit on the latter as:

$$(N - N')(t) = A \exp\left(-\frac{t - t_0}{\tau}\right) \tag{3.7}$$

If we differentiate this expression, we get:

$$\frac{d(N - N')(t)}{dt} = -\frac{A}{\tau} \exp\left(-\frac{t - t_0}{\tau}\right) \tag{3.8}$$

Now we can make the approximation that this derivative in the first 100 μs is constant and is equal to $\frac{d(N-N')(t=0)}{dt} = -\frac{A}{\tau}$. Finally, we substitute N_{tar} using (3.1) and we obtain:

$$\frac{dN_{tar}}{dt} = -\frac{A}{\tau\alpha} \exp\left(-\frac{t - t_0}{\tau}\right) \tag{3.9}$$

Therefore, Γ_{BBR} rates can be corrected as follows:

$$\Gamma_{BBR} = \frac{dN_{supp}}{dt} = \frac{dN'}{dt} + \frac{(1-\alpha)}{\alpha}\frac{A}{\tau} \tag{3.10}$$

In Figure 3.5 the BBR rates corrected of S and P states are shown. The differences from the BBR rates of the target method are reduced, although the P state rates show still discrepancy from the BBR rates of the target method. However, one may observe how the corrected BBR rates follow more the trend of the BBR rates of the other method. For the S state rates, on the other hand, the correction resulted in small changes, as the depumping efficiency was always above 90%. The main results of this chapter are based on measurements of S-state lifetimes, so this correction was not applied.

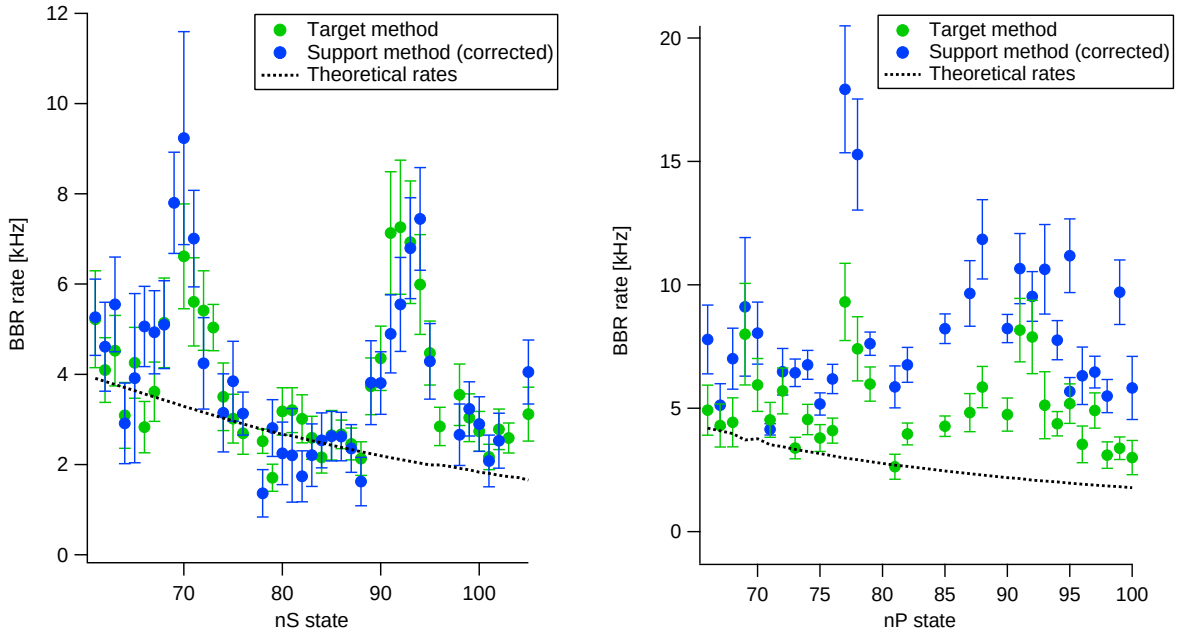

Figure 3.5: The BBR rates of S (left side) and P (right side) states calculated with the support method, taking into account the correction for low depumping efficiency (in blue). The results are compared to the BBR rates calculated with target method and the theoretical BBR rates.

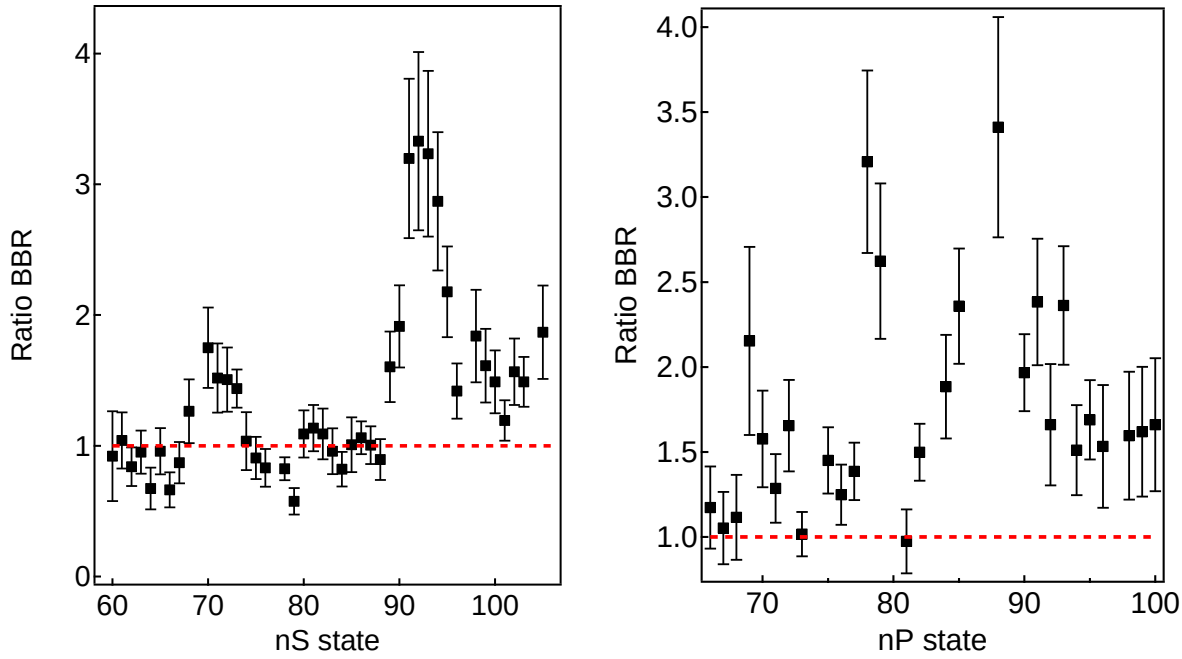

Figure 3.6: Ratio between the experimental BBR rates of S (left-side) and P (right-side), calculated with the target method and the theoretical BBR rates, calculated with the ARC[21] libraries. The data are clearly showing significant deviations, mainly localized around nS states with $n = 70$ and $n = 90$.

We evaluated the ratio between the experimental BBR rates calculated with the target method and the theoretical BBR rates of both S and P (Figure 3.6), and confirmed the deviations of BBR rates from the theoretical rates.
The main deviations of the BBR rates correspond to two frequency intervals, that range from 4 to 5 GHz and from 9 to 11 GHz. We created therefore a model of the density of modes deduced by the measured lifetimes that is explained in the following section.

3.4.2 Expected lifetimes model

Firstly, we can qualitatively express the deviations with the following expression[10]:

$$D(\nu,\{\beta\}) = \frac{\rho_{model}(\nu,\{\beta\})}{\rho_{Theo}(\nu)} = 1 + a_1\frac{\Delta\nu_1}{(\nu-\nu_1)^2+\Delta\nu_1^2} + a_2\frac{\Delta\nu_2}{(\nu-\nu_2)^2+\Delta\nu_2^2} + a_3\frac{\Delta\nu_3}{(\nu-\nu_3)^2+\Delta\nu_3^2}, \tag{3.11}$$

that consists of three Lorentzian functions where $\rho_{model}(\nu,\{\beta\})$ is the density of modes of the model, $\rho_{Theo}(\nu)$ is the density of modes calculated with Planck's formula and $\{\beta\} = \{a_1, a_2, \nu_1, \nu_2, \Delta\nu_1, \Delta\nu_2\}$ is a set of coefficients. Observing that each BBR transition rate (1.10) is linear with the density of modes, we can modify these rates as:

$$\Gamma_{nlj}^{(model)} = \sum_{n'l'j'} \Gamma_{nlj,n'l'j'}^{(BBR)} D(\nu_{nlj,n'l'j'},\{\beta\}) \tag{3.12}$$

Finally, we perform an iteration routine on the $\{\beta\}$ parameters minimizing the difference between each experimental lifetime and the lifetime calculated with the model, that is:

$$\tau_{nlj}^{(model)} = \left(\Gamma_{nlj}^{(spon)} + \Gamma_{nlj}^{Model}(\{\beta\})\right)^{-1} \tag{3.13}$$

This minimization was performed on both S and P states and yielded the result shown in Figure 3.7.

We attributed these BBR rates deviations to the influence of the finite size of the silica cell. In fact, the frequencies of the BBR-induced transitions for the states that have the greater deviations from the theoretical lifetimes are comparable to the low modes of a resonant cavity with the dimensions of the fused silica cell (the description of the geometry of the cell is in section 2.6.1), which may cause these enhancements in the BBR spectrum.
Let's consider for simplicity a two dimensional resonant cavity along the y and z axes:

$$f_{n_y,n_z} = \frac{c}{2}\sqrt{\left(\frac{n_y}{L_y}\right)^2 + \left(\frac{n_z}{L_z}\right)^2}, \tag{3.14}$$

and consider the shortest external dimensions of the cell, i.e. $L_y = 30\,\text{mm}$ and $L_z = 24\,\text{mm}$. The associated resonant mode with $n_y = 1$ and $n_z = 0$ is equal to $f_{1,0} = 5\,\text{GHz}$, which is comparable with the second peak from the left in Figure 3.7. While, if the internal dimensions of the cell are considered, which are $L_y = 24\,\text{mm}$ and $L_z = 18\,\text{mm}$, and the $f_{1,1}$ mode, this is equal to about $10.42\,\text{GHz}$, that is comparable to the third peak. For the first peak, on the other hand, we didn't find any resonance associated either to the cell or other surrounding elements of the apparatus.
In the end, to ensure that these enhancements were not caused by any external signals, like Wi-Fi or radar signals, a Faraday cage made of Aluminium was built around the apparatus[10]. We ensured that this cage reflected sufficiently the electromagnetic waves. No difference in the lifetime measurements was observed with this configuration.

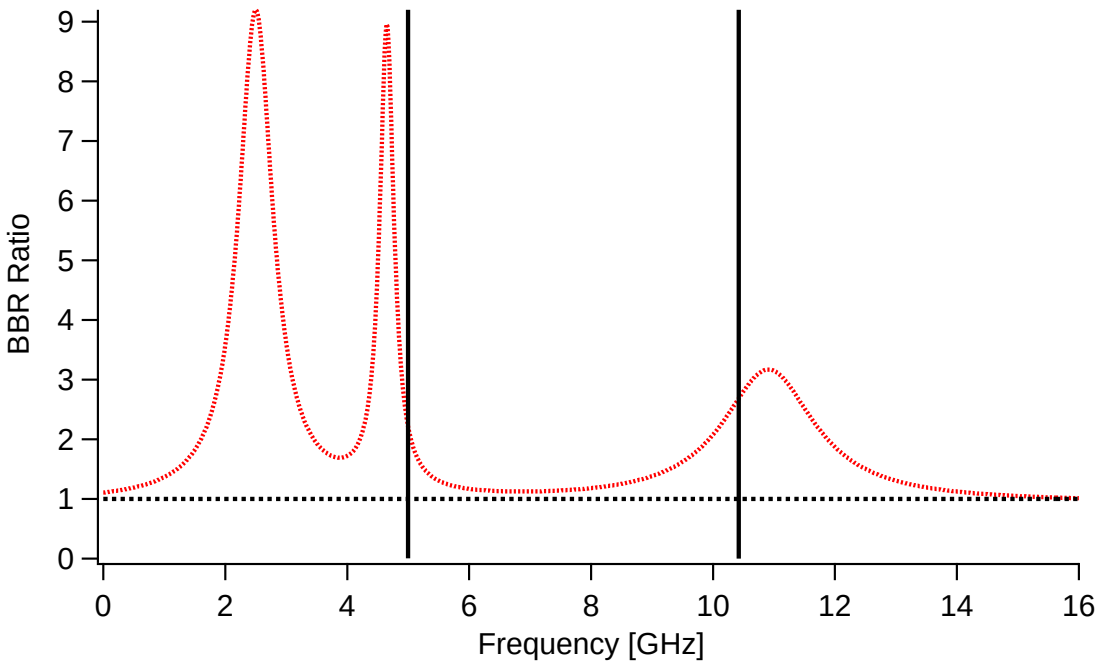

Figure 3.7: The resulting expression $D(\nu, \{\beta\})$ (3.11) obtained by the minimization routine applied on S and P state lifetimes. This trend is compared with resonant modes of the resonant cavity that we associated to the silica cell.

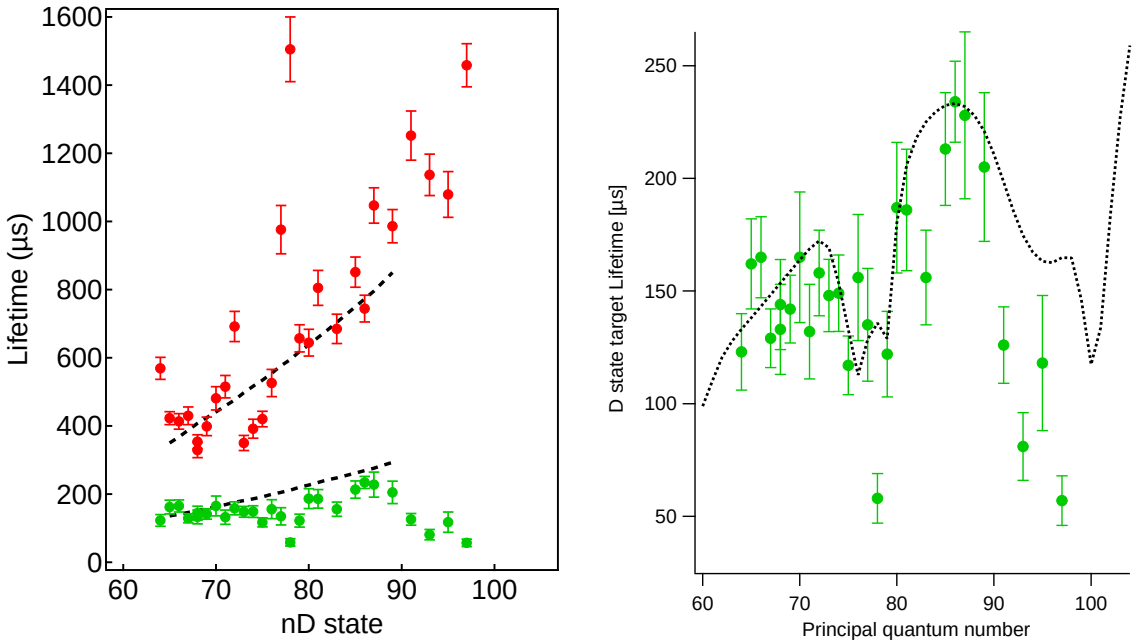

Figure 3.8: On the left side D state ensemble and target lifetimes (respectively in green and red), compared to the theoretical values (black dashed lines). On the right-side D state target lifetimes compared to the fit obtained by the S and P states measurements.

3.5 D state lifetimes measurement

I spent the first period of my experimental work on the measurements of the nD states with $J = 5/2$ lifetimes on a range of n from 64 to 97. The goal of this set of measurements was to confirm the deviations of the experimental lifetimes in the same frequency ranges observed in the S and P measurements.

All the measurements were taken with a residual electrical field magnitude such that all states were well below the Inglis-Teller limit (Stark shift section 1.2.1). However, we found that the target lifetime measurements could vary up to factor of 2 as a function of the electric field magnitude (Figure 3.9). Even if we did not exactly know the causes of this phenomenon, we made sure that all D states lifetime measurements were taken with residual fields magnitudes below 40 mV/cm.

We translated the modes spectrum obtained by the model of section 3.4.2 in this expected D states lifetimes. In the right side of Figure 3.8 the expected trend of the lifetimes is compared to the experimental data. For the states with n from 65 to 89, The experimental values are mostly in good agreement with the values obtained by the model. However, the lifetimes of states with greater

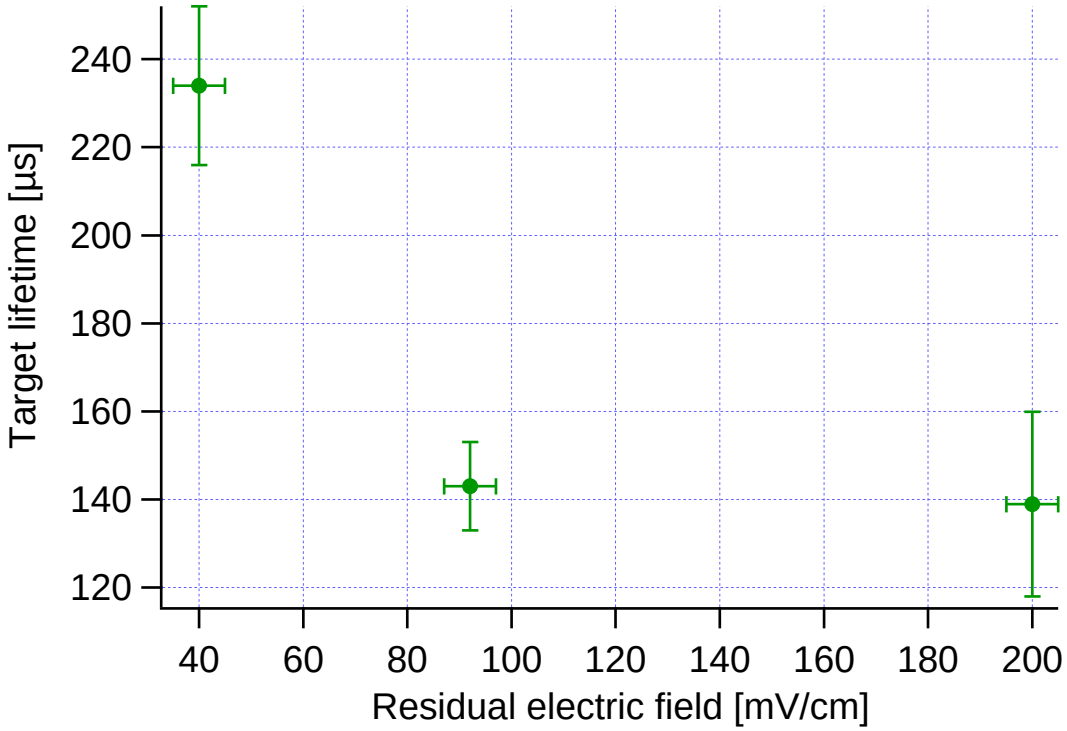

Figure 3.9: Target lifetime of the $86D$ state measured with different magnitudes of the residual electric field (Inglis-Teller limit for $86D$ state is at $E \sim 300\,\mathrm{mV/cm}$). Note how the values at $E \sim 40\,\mathrm{mV/cm}$ and $E \sim 80\,\mathrm{mV/cm}$ differ by almost a factor of 2.

principal quantum number are significantly lower than expected. This could be attributed to higher sensitivity to the electric field mentioned before, as the dipole matrix elements grows with n.

3.6 Modification of Rydberg state lifetimes

3.6.1 Mode density model

In order to understand how the meshes and the Aluminium plates implemented in the apparatus changed the spectrum of the density of modes inside the cavity, we designed a theoretical model of the density of modes inside the cavity.

The calculation follows to some extent the one done for an ideal resonant cavity, which I already shown in section 1.4.1, defining L_x, L_y and L_z as the three dimensions of the cavity. Regarding the third cavity dimension along the x axis, this is necessary to compare the mode density of the

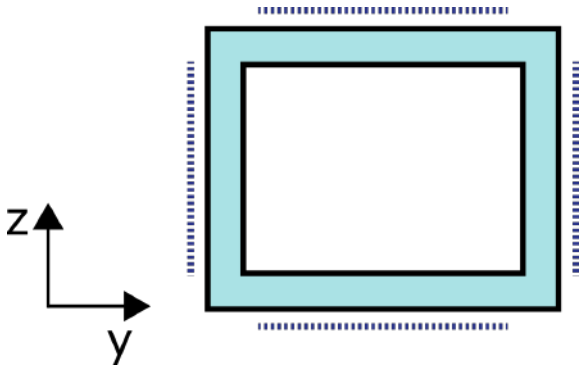

Figure 3.10: Section of the cell on the yz plane with the meshes placed nearby.

cavity with the one of the black body radiation of a rectangular box with the same dimension of the resonating cavity. The x dimension was chosen to be great enough, about 300 mm, such as it did not contribute significantly to the cavity modes. We have to take into account the presence of the fused silica cell. The cell walls are 3 mm wide and are oriented inside the meshes cavity as it can be seen in Figure 3.10. The silica glass has clearly a refractive index different from the air in the microwaves range of our experiments. Unfortunately we found very few papers concerning the measurements of the refractive index of such materials in frequencies close to the ones of our experiments[37]. We found in literature values ranging from $n = 2$ to $n = 2.6$ for the frequencies. This unknown variable can change substantially the results, so we performed various calculations with different values of the refractive index, to see which one seemed to be more consistent with the experimental results. To simplify the model, we calculated for each fundamental mode an average refractive index weighted by the thickness of the glass and the width of the space occupied by air between each pair of cavity walls:

$$\overline{n}_i = \frac{n_{glass} w_{glass} + n_{air} w_{air,i}}{L_i}, \quad w_{air,i} = L_i - w_{glass}, \quad i = x, y, z, \tag{3.15}$$

The fundamental harmonics therefore become

$$\nu'_x = \nu'_{1,0,0} = \frac{c}{2\overline{n}_x}\frac{1}{L_x} \quad \nu'_y = \nu'_{0,1,0} = \frac{c}{2\overline{n}_y}\frac{1}{L_y} \quad \nu'_z = \nu'_{0,0,1} = \frac{c}{2\overline{n}_z}\frac{1}{L_z}, \tag{3.16}$$

thus the higher harmonics can be expressed as

$$\nu'_{m_x,m_y,m_z} = 2\sqrt{(m_x\nu'_x)^2 + \left(m_y\nu'_y\right)^2 + (m_z\nu'_z)^2}, \tag{3.17}$$

where each mode is counted twice to take into account both possible polarizations of the electromagnetic waves in the cavity.

The next step was to calculate the density of modes inside the cavity within the frequency range of

the transitions of the Rydberg states considered in our experiments, and to compare it to the mode density of Planck's black body radiation formula. I calculated with (3.17) all the modes with n_x, n_y and n_z with the rules already shown in section 1.4.1. I required that the resulting frequencies were less than 10 GHz, that is approximately the maximum frequency of BBR-induced transitions between the states considered in my measurements. This operation was made by holding fixed two of the mode numbers and varying another one, then changing one of the fixed numbers, until determined values were reached by each mode number. These determined values were chosen to be sure that all the resonant modes of the cavity were counted in the range of 0 to 10 GHZ. The frequency range was divided in intervals of $\Delta\nu = 500$ Mhz. This frequency interval is approximately equal to the broadening of the resonant frequencies that we have if we assume a quality factor of the cavity of about 10 (section 1.4.2). This can be seen if we consider an average frequency of $\nu = 5$ GHz, as we got $\Delta\nu = \nu/Q = 500$ MHz. I counted together the modes that stayed in the same interval.
Regarding the mode density calculated with Planck's formula, I took the expression for the number of modes at frequency ν in a frequency interval $\nu + \Delta\nu$ within a volume $V = L_x L_y L_z$. In the expression we must consider the contribution of the average refractive index for each dimension. So, we get:

$$\Delta\nu_{Planck} = V 8\pi\nu^2 \Delta\nu \frac{\overline{n}_x \overline{n}_y \overline{n}_z}{c^3}. \tag{3.18}$$

Finally I plotted the results for different dimensions of the cavity as histograms shown in Figure 3.11, where the number of modes in each interval is divided by the one obtained by Planck's formula (see BBR section 1.3 in the theoretical background chapter). The presence of the cut-off frequency is evident, although its precise position in the frequency spectrum depends strongly on the value of the refractive index of the glass in the frequency range from about 3 to 10 GHZ, for which we found values between 2 and 2.6 in the literature. Moreover, for certain configurations of cavity dimension, it is possible to have modes suppressions in some regions above the cut-off frequency (In the case of the histograms shown on the left side of Figure 3.11, in the interval from 4 to 4.5 GHz). However, we observed that these regions are very sensitive to the cavity dimensions. In fact, it is sufficient that both of the y and z dimensions were shifted by 1 mm to lose the regions of suppressed modes[1] (right side of Figure 3.11).

[1] This distance is practically equal to the precision we have on changing the cavity dimension.

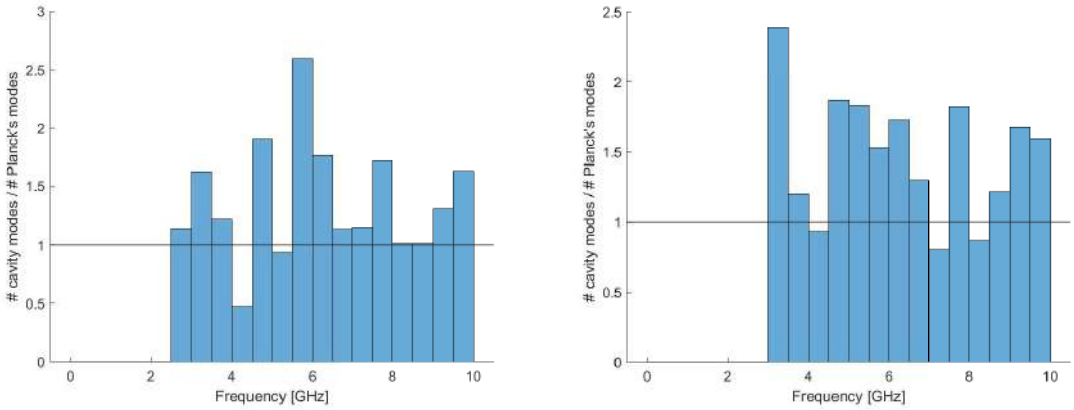

Figure 3.11: Two histograms showing the number of modes per frequency width $\Delta\nu = 500\,\text{GHz}$ calculated for a refractive index of the fused silica glass of $n_{glass} = 2$ and a cavity with $L_x = 300\,\text{mm}$, $L_y = 45\,\text{mm}$ and $L_z = 26\,\text{mm}$ on the left side. On the right side the calculation is performed again with the same parameters but $L_y = 43\,\text{mm}$ and $L_z = 28\,\text{mm}$. The number of modes is divided by the number of modes of Planck's formula for the BBR. As can be seen, the

3.6.2 Measurements with meshes

All the experiments were performed with nS Rydberg states. The first measurements were carried out with the two pairs of meshes described in section (2.6.2). The pair that acted as vertical walls of the cavity were initially $15 \times 18\,\text{mm}$ wide. We placed the meshes and performed measurements with different lengths of each one of the two cavity dimensions, while the other one was held in a fixed position. For each position I performed a lifetime measurement of the same Rydberg state as sample, namely the state with $nL = 93S$. From the measurement I calculated the BBR rates with the two methods explained in section (3.3). The results can be seen in Figure 3.12.
Let's overlook momentarily the difference between the two sets of rate calculated with the two methods, which will be analysed later. The variation in the dimensions of the cavity did not particularly affect the BBR rates, as for each measurement performed with a different dimension the BBR rates calculated with the two methods agreed to each other within their errors bars. This means that the density of modes around the frequency associated to that Rydberg state remained constant for each configuration of the cavity.

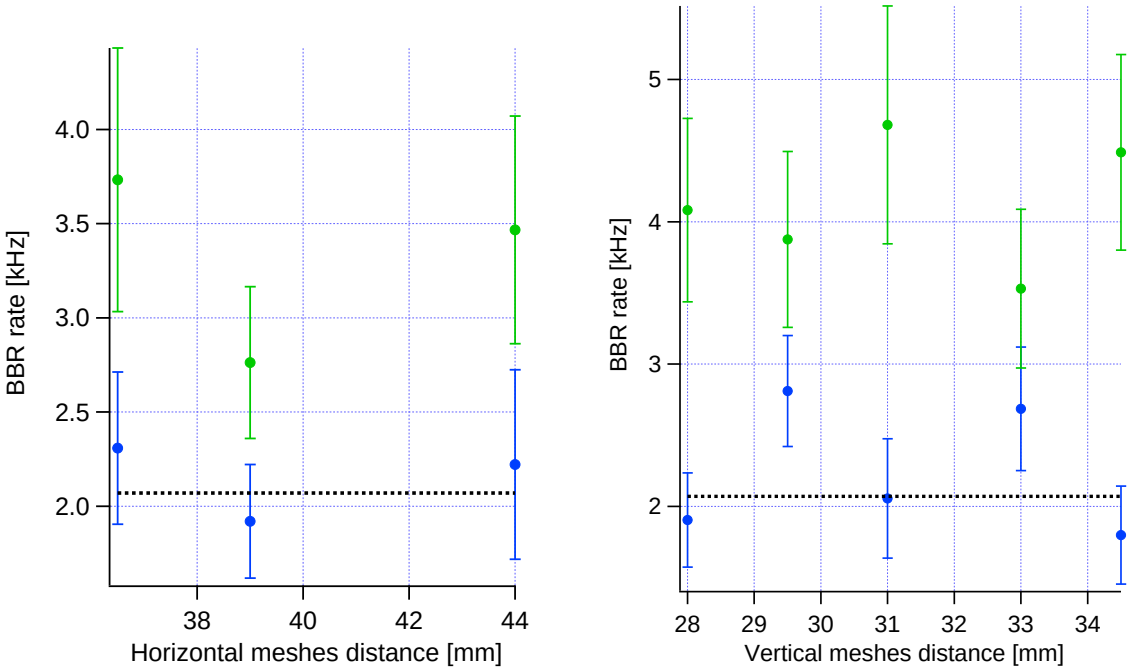

Figure 3.12: On the left side the BBR rate of the Rydberg $93S$ state as a function of different horizontal distances of the cavity and with the same vertical distance of 26 mm. On the right-side the BBR rate of the same state but in function of different vertical distances of the cavity and with the same horizontal distance of 37 mm. Each BBR rate is calculated with the support method (in blue) and the target method (in green), compared to the theoretical value (black dashed line).

3.6.3 Measurements with meshes and Aluminium plates

After these set of measurements with different cavity lengths, we improved the quality factor of the cell by extending the vertical walls, i.e the surfaces of the meshes placed vertically. The new dimensions were 60×18 mm. Moreover, the Al plates described in section 2.6.3 were added to the apparatus, extending in this way the horizontal walls of the cavity to about 12 cm along the y axis. With this setting I performed experiments with different lengths of the horizontal dimension by shifting the positions of the vertical meshes, while the horizontal ones were kept at the minimum distance. i.e. 26 mm. From the lifetime measurements I calculated the BBR rates as for the previous set of measures (Figure 3.13). None of those measurements yielded any significant suppression of the BBR rates, but only enhancements.

As can be seen from Figure 3.12 and Figure 3.13, the BBR rates calculated with the support method are mostly below the ones calculated with the target method, unlike the results of the S states without the meshes and Aluminium plates placed in the apparatus. It can be observed that

the BBR rates differ not simply by an offset, but actually show different trends, as can be noticed for instance in the measurements with the vertical meshes at 42 mm (Middle right graph in Figure 3.13).

We don't know exactly the reason of these differences, but we hypothesize that they may depend on the fact that the support method yields a local BBR rate, as it is calculated on the first times of the system evolution (section 3.3.1). If we have a non-uniform BBR transition rate along the overall duration of the measurement, the BBR rate in this way can be no longer considered valid. Let's consider, for instance, a fast decay of the target population in the early evolution times, and then a slowdown of the decay for longer times. This means that with the support method a greater rate is calculated. By contrast, the target method (section 3.3.2) is calculated using the global total rate and therefore yields an average of the BBR rate during the evolution of the system. Further analysis of this result are being conducted at the same time this thesis is being written.

3.6.4 Conclusions

With the experiments that I carried out with the addition of the microwave resonant cavity I was able to characterize the mode density of each configuration of the cavity. I observed significant changes in the mode density for different configurations the cavity dimension. I proved that it is possible to change Rydberg lifetimes from the values measured without the resonant cavity. For instance, in Figure 3.14 a set of Rydberg state lifetimes for a certain configuration is shown, where the difference from the Rydberg lifetimes without the cavity and the ones with the cavity is significant. In fact, for this configuration a new enhancement resonance of the BBR rate was found for S states with n in the range from $n = 98$ to $n = 105$, where the measured lifetimes are visibly smaller than the lifetimes without the resonant cavity.

However, I was unable to find a region where BBR-induced transitions of Rydberg states are suppressed, i.e. an extension of the lifetimes beyond the theoretical values. This is not entirely surprising, as from the mode density calculation (section 3.6.1) we predicted that finding a region above the cut-off frequency would be difficult because of the sensitivity of the resonant cavity to variations in its dimensions.

Furthermore, we were also not able to measure Rydberg states whose BBR-induced transitions were below the cut-off frequency. We hypothesize that, for the low Q factor we estimated (section 1.4.2), the trend of the cut-off frequency might be significantly broadened. So even if the cut-off frequency had been in the range of frequencies associated to the measured Rydberg states, its broadening would not have allowed us to observe any modes suppression. From our results, we expect that a suppression of the density of modes might be observable for Rydberg S-states with n well above 110. However, lifetime measurements of these Rydberg states are impossible for our apparatus,

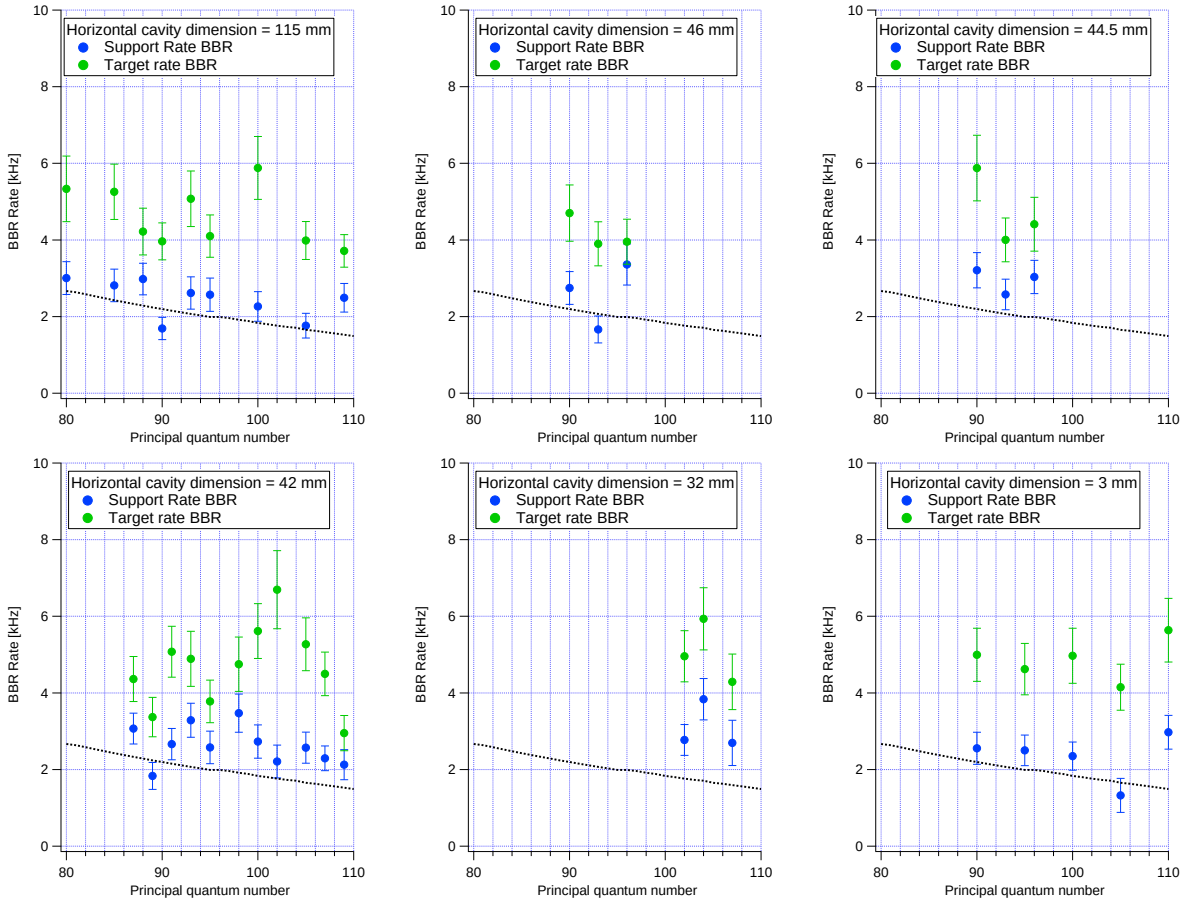

Figure 3.13: BBR rates for the Rydberg state lifetimes measured with each distance of the horizontal cavity. Each BBR rate is calculated with the support method (in blue) and the target method (in green), compared to the theoretical values (black dashed line).

since for the minimum background electric field we could achieve with our compensation technique (section 2.5), those states are already mixed with the manifold.

Further modifications of the resonant cavity in order to extend the walls of the cavity may lead to an increase of the Q factor. For instance, the vertical walls, that consist only of the meshes (section 2.6.2), might be extended with additional Aluminium plates placed on the side of the frames of the mesh. In this way, one shall induce the formation of extended suppression regions of the mode for the frequencies associated to the BBR transition rates of individual nS Rydberg states, and therefore the extension of the lifetimes of these states.

A possible way to carry out investigations for the use of the resonant cavity to finally extend Rydberg state lifetimes could be the design of a "dummy" of the resonant cavity. This model could be built using the same meshes applied to the apparatus and have a layer of glass to simulate the presence

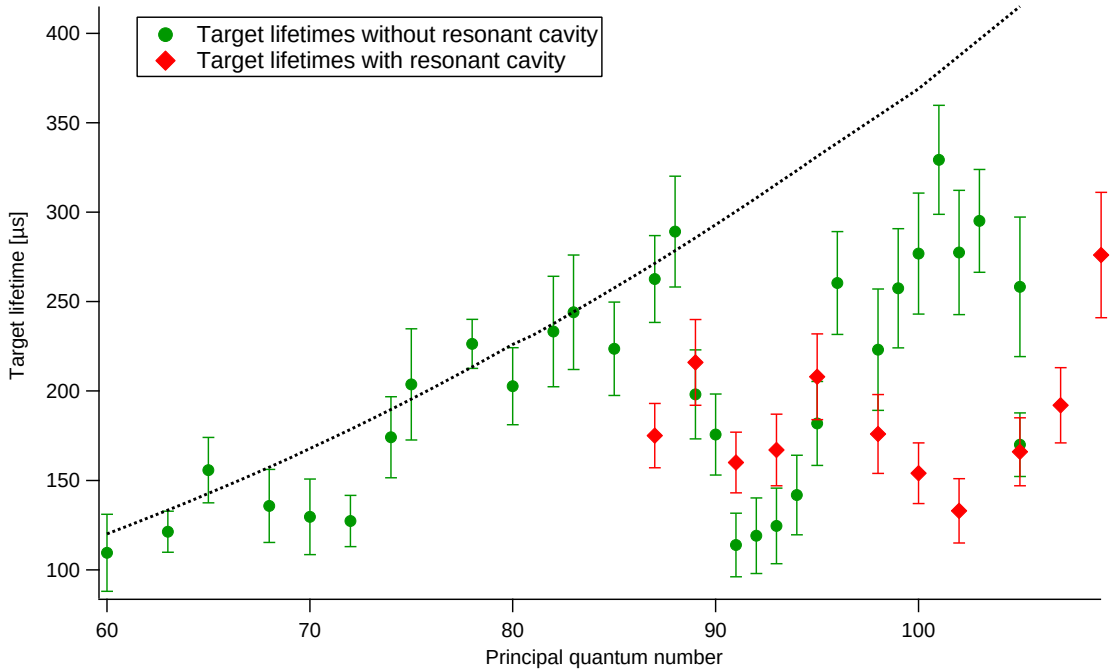

Figure 3.14: Set of Rydberg state lifetimes measurements taken with the final configuration of the resonant cavity, i.e. with the presence of meshes and Aluminium plates (red diamonds), compared to the previous measurements without the resonant cavity yet (in green) and the theoretical values (black dashed line). The separation of the vertical meshes was at a distance of 42 mm, while the separation of the vertical meshes was 26 mm.

of the silica cell. It could be possible to perform independent measurements of the mode density spectrum on this model using a microwave generator and a spectrum analyzer. These measurements would allow us to characterize the mode spectrum, the quality factor and the influence of the glass on the mode density in such cavities.

Chapter 4

Conclusion

This thesis reports two sets of experimental studies on lifetimes of Rydberg atoms. The first set regarded the experimental measurements of Rydberg D state. The second set regarded the implementation of a resonant microwave cavity in the apparatus and the measurements of the subsequent changes of Rydberg S state lifetimes.
I explained the lifetime measurement technique used for both sets of experiments, which consists of excitation, de-excitation of single Rydberg lifetimes and following field ionization. I showed the two calculation methods for rates of black body induced transitions, pointing out the differences and the approximations made in each method.
The results of the D state lifetimes showed a good agreement with the results of both S and P state lifetimes, confirming the deviations of the density of modes of the black-body radiation experienced in the states with lower angular momenta for most of the states measured. However, the D state lifetimes exhibit a higher sensitivity to the electric field, even if the Rydberg levels are not mixed. Therefore I observed lower lifetimes of D state with highest n, because of their stronger coupling with the electric field. The analysis of this behaviour is left as an outlook and is not included in my work.
For each S, P and D state lifetimes I calculated the rates of black body induced transitions with the support method, finding a good agreement with the target method for the S states, while for the P states I observed some discrepancies between the results of the two methods. The differences were reduced by applying a correction on the calculation of the BBR rates from the support, that took into account the low depumping efficiency in the P state measurements.
Regarding the second and more substantial part of my experiments, I designed, built and placed the elements that formed the two dimensional resonating cavity around the MOT. I measured different sets of Rydberg lifetimes for each configuration of the cavity, varying both cavity lengths. In this way I characterized the mode density for each configuration, observing significantly changes between the measured lifetimes and the lifetimes measured before the implementation of the cav-

ity. Therefore I proved the possibility to change Rydberg lifetimes with the sole application of a resonant microwave cavity. From each lifetime measurement I calculated the rates of black body induced transitions with both methods. The results of the two methods are significantly different from each other and the reason of that is object of analysis in the period of time when this thesis is being written.

A simplistic model of the mode density has been designed. In this model we calculated the mode density of resonant cavity with the same dimension of the cavity placed in the apparatus. We took into account the presence of the silica cell with an average refractive index, but not the fact that we are dealing with an open resonating cavity. Finally we compared the resulting modes spectrum with the one calculated with the Planck's formula for a volume with the same dimensions of the resonant cavity. We observed that, for some configurations of the dimensions, regions with mode density below Planck's mode density appeared. Those regions, however, were although highly sensitive to the dimensions of the apparatus. Thus we concluded that such configurations were difficult to produce with the precision we had on adjusting the dimensions of the resonant cavity. Moreover, modifying the actual configuration of the resonant cavity in order to increase the Q factor may ease the formation of suppressed modes in the frequency spectrum.

Further studies shall include experiments with a "dummy" microwave cavity similar to the one placed in the apparatus, which can be used to perform measurements of its resonances. Those measurements could help to better understand the mode density of the main resonant cavity and hopefully find favourable conditions with which to observe a reduction of the BBR-induced transition rates, and hence an enhancement of the lifetimes of the Rydberg states.

Bibliography

[1] I. M. Georgescu, S. Ashhab, and F. Nori, "Quantum simulation," *Rev. Mod. Phys.*, vol. 86, pp. 153–185, 03 2014.

[2] "Hewlett-Packard labs, The Machine." https://www.labs.hpe.com/memory-driven-computing.

[3] R. P. Feynman, "Simulating physics with computers," *International journal of theoretical physics*, vol. 21, pp. 467–488, 1982.

[4] I. Buluta and F. Nori, "Quantum Simulators," *Science*, vol. 326, no. 5949, pp. 108–111, 2009.

[5] H. Weimer, M. Müller, I. Lesanovsky, P. Zoller, and H. P. Büchler, "A Rydberg quantum simulator," *Nature Physics*, vol. 6, p. 382–388, 03 2010.

[6] M. Valado, C. Simonelli, M. Hoogerland, I. Lesanovsky, J. Garrahan, E. Arimondo, D. Ciampini, and O. Morsch, "Experimental observation of controllable kinetic constraints in a cold atomic gas," *Phys. Rev. A*, vol. 93, p. 040701, 08 2015.

[7] T. F. Gallagher and W. E. Cooke, "Interactions of blackbody radiation with atoms," *Phys. Rev. Lett.*, vol. 42, pp. 835–839, 03 1979.

[8] M. Archimi, *Experimental studies of the blackbody induced population migration in dissipative Rydberg systems*. PhD thesis, University of Pisa, 2019.

[9] L. D. Virgilio, "Characterization and compensation of stray electric fields in cold Rydberg atom experiments," Master's thesis, University of Pisa, 2019.

[10] M. Ceccanti, "Experimental characterization of blackbody induced transitions in high-lying Rydberg states," Master's thesis, University of Pisa, 2019.

[11] A. Greco, "Experimental studies of the lifetimes of Rubidium Rydberg atoms as sensors of blackbody radiation," Master's thesis, University of Pisa, 2019.

[12] D. Branden, T. Juhasz, T. Mahlokozera, C. Vesa, R. Wilson, M. Zheng, A. Kortyna, and D. Tate, "Radiative lifetime measurements of Rubidium Rydberg states," *Journal of Physics B: Atomic, Molecular and Optical Physics*, vol. 43, p. 015002, 12 2009.

[13] L. Marcassa, "Measurement of Rydberg state lifetimes using cold trapped neutral atoms," *Physica Scripta*, vol. 2009, p. 014011, 05 2009.

[14] M. Mack, J. Grimmel, F. Karlewski, L. Sárkány, H. Hattermann, and J. Fortágh, "All-optical measurement of Rydberg state lifetimes," *Phys. Rev. A*, vol. 92, 07 2015.

[15] M. Archimi, C. Simonelli, L. Di Virgilio, A. Greco, M. Ceccanti, E. Arimondo, D. Ciampini, I. Ryabtsev, I. Beterov, and O. Morsch, "Measurements of individual and ensemble lifetimes of high-lying Rb Rydberg states," *Phys. Rev. A*, p. 030501(R), 07 2019.

[16] K. Lai and E. Hinds, "Blackbody excitation of an atom controlled by a tunable cavity," *Phys. Rev. Lett.*, vol. 81, pp. 2671–2674, 09 1998.

[17] F. Meinert, C. Hölzl, M. Nebioglu, A. D'Arnese, P. Karl, M. Dressel, and M. Scheffler, "Indium tin oxide films meet circular Rydberg atoms: Prospects for novel quantum simulation schemes," *Physical Review Research*, vol. 2, p. 023192, 05 2020.

[18] A. Reiser and L. Schächter, "Geometric effects on blackbody radiation," *Phys. Rev. A*, vol. 87, p. 033801, 03 2013.

[19] T. H. Gallagher, *Rydberg Atoms*. Cambridge University Press, 1994.

[20] R. Löw, H. Weimer, J. Nipper, J. B. Balewski, B. Butscher, H. P. Büchler, and T. Pfau, "An experimental and theoretical guide to strongly interacting Rydberg gases," *Journal of Physics B: Atomic, Molecular and Optical Physics*, vol. 45, p. 113001, 05 2012.

[21] N. Šibalić, J. Pritchard, C. Adams, and K. Weatherill, "Arc: An open-source library for calculating properties of alkali Rydberg atoms," *Computer Physics Communications*, vol. 220, pp. 319–331, 09 2017.

[22] D. Griffiths, *Introduction to Quantum Mechanics*. Prentice Hall, Inc., 1995.

[23] S. Blundell, S. Blundell, and K. Blundell, *Concepts in Thermal Physics*. Oxford University Press, 2006.

[24] S. Rytov, *Theory of Electric Fluctuations and Thermal Radiation*. Air Force Cambridge Research Center, 1959.

[25] J. D. Jackson, *Classical electrodynamics; 2nd ed.* Wiley, 1975.

[26] D. Pozar, *Microwave Engineering, 4th Edition*. Wiley, 2011.

[27] K. J. Coakley, J. D. Splett, M. D. Janezic, and R. F. Kaiser, "Estimation of Q-factors and resonant frequencies," *IEEE Transactions on Microwave Theory and Techniques*, vol. 51, no. 3, pp. 862–868, 2003.

[28] X. Ge and S. He, "Experimental realization of an open cavity," *Scientific reports*, vol. 4, pp. 59–65, 08 2014.

[29] H. J. Metcalf and P. van der Straten, *Laser Cooling and Trapping*. Springer, 1999.

[30] K. Kowalski, C. Van, D. Khoa, M. Głódź, B. Nguyen, and J. Szonert, "Magneto-optical trap: Fundamentals and realization," *Computational Methods in Science and Technology*, vol. Special Issue, pp. 115–129, 01 2010.

[31] J.-H. Choi, B. Knuffman, T. Liebisch, A. Reinhard, and G. Raithel, "Cold Rydberg atoms," *Advances In Atomic, Molecular, and Optical Physics*, vol. 54, pp. 131–202, 01 2006.

[32] F. J. Deck, E. A. Hessels, and S. R. Lundeen, "Population of high-L sulfur Rydberg levels by ion-Rydberg-atom charge exchange," *Phys. Rev. A*, vol. 48, pp. 4400–4404, 12 1993.

[33] D. C. Cartwright, W. J. Hunt, W. Williams, S. Trajmar, and W. A. Goddard, "Theoretical and experimental (electron-impact) studies of the low-lying Rydberg states in o_2," *Phys. Rev. A*, vol. 8, pp. 2436–2448, 11 1973.

[34] M. Viteau, J. Radogostowicz, A. Chotia, M. G. Bason, N. Malossi, F. Fuso, D. Ciampini, O. Morsch, I. I. Ryabtsev, and E. Arimondo, "Ion detection in the photoionization of a Rb Bose–Einstein condensate," *Journal of Physics B: Atomic, Molecular and Optical Physics*, vol. 43, pp. 155–301, 07 2010.

[35] L. Deputatova, V. Filinov, D. Lapitsky, V. Pecherkin, R. Syrovatka, L. Vasilyak, and V. Vladimirov, "Measurement of the charge of a single dust particle," *Journal of Physics: Conference Series*, vol. 653, pp. 012–129, 11 2015.

[36] A. Reinhard, T. Cubel Liebisch, K. C. Younge, P. R. Berman, and G. Raithel, "Rydberg-Rydberg collisions: Resonant enhancement of state mixing and Penning ionization," *Phys. Rev. Lett.*, vol. 100, p. 123007, 03 2008.

[37] J. Birch, R. Cook, A. Harding, R. Jones, and G. Price, "The optical constants of ordinary glass from 0.29 to 4000 cm-1," *Journal of Physics D: Applied Physics*, vol. 8, p. 1353, 01 2001.